ECAP-2017-010

Applications of Dual Energy Phase Contrast X-Ray Imaging

Master's Thesis in Physics

Presented by

Theresa Palm

March 23, 2017

performed at

Erlangen Centre for Astroparticle Physics
Friedrich-Alexander-Universität Erlangen-Nürnberg

Supervisor: Prof. Dr. G. Anton

ERLANGEN CENTRE FOR ASTROPARTICLE PHYSICS

FRIEDRICH-ALEXANDER UNIVERSITÄT ERLANGEN-NÜRNBERG

Contents

Introduction

Radiography and Computed Tomography (CT) are standard imaging methods in medical practice that have become established as indispensable tools in diagnostics. In recent years, the field of applications of these tools has been expanded by making use of information from two radiographic images obtained at different photon energies [1]. This so-called Dual Energy radiography can be used to identify materials [2], visualise veins [3], analyse bone mineral [4] and calculate body fat percentages [5–8]. While in conventional radiography only the attenuation values of an object are imaged, the method of phase-contrast X-ray interferometry provides additional information. Using a Talbot-Lau interferometer, phase-contrast imaging measures phase shift and dark-field signals of objects in addition to their attenuation properties [9–12]. These qualities are particularly interesting for medical purposes, as the differential phase image has higher soft tissue contrast than the attenuation image. The latter is suited best for bone measurements. The idea this thesis is based on, is to combine the advantages of phase-contrast X-ray interferometry with the benefits of Dual Energy measurements.

Therefore, in the first part of this thesis, phase-contrast CT measurements of several objects are carried out at different energies. For the analysis of the resulting images, an algorithm is implemented that allocates pixels to known materials based on the material information obtained in the Dual Energy measurements. This way, more than two materials, like in conventional Dual Energy radiography, can be identified. Firstly, this method is tested on a sample made of plastic rods, then it is transferred to a more complex structure. Finally, as a typical application of conventional Dual Energy CT, the fat percentage of a biological sample is determined using the algorithm in order to assess the possibilities of phase-contrast Dual Energy CT.

In the second part, renal calculi (kidney stones) are examined with phase-contrast radiography. Kidney stone disease is very common in countries with a high standard of living and its prevalence is increasing [13]. Renal calculi can be composed of different minerals, which can occur in pure form or as a mixture of different minerals. There are several non-invasive treatment methods that only work on stones of a particular mineral composition [14, 15]. Currently, Dual Energy CT is used in clinical practice to identify Uric acid, one of the minerals in question [16]. Based on the knowledge of the material, an appropriate treatment method can be chosen. Previous publications on phase-contrast radiography have shown that Uric acid differs from the other kidney stone minerals in its attenuation and dark-field values [17]. In this thesis, projective phase-contrast measurements are carried out in order to examine if these results can be confirmed. Apart from Uric acid, there are more minerals (like Cystine, Brushite and Whewellite) with properties that are relevant for the decision on a treatment method that cannot be identified unambiguously yet by Dual Energy CT. Carrying out phase-contrast CT measurements of the kidney stones, it is investigated whether the refractive index in combination with the dark-field and attenuation coefficient is suitable for the differentiation of minerals.

Chapter 1

Physical Fundamentals

Contents

For a better understanding of the physics of interferometric X-ray imaging, its physical principles are presented in this chapter. Firstly, X-rays are introduced as electromagnetic waves. For imaging purposes it is vital to know the interaction behaviour of the incident waves with the material, which is discussed subsequently. Secondly, the set-up of a Talbot-Lau interferometer is explained as well as the different images that can be obtained using it.

1.1 X-rays

X-ray imaging is based on interaction of electromagnetic waves with matter. The wavelengths of X-rays lie in the regime of 10^{-8} m to 10^{-12} m. A spatially resolving detector can be used to measure the change in intensity of the wave that has passed the object. That way, one can draw conclusions on the composition of the measured object.

1.1.1 Electromagnetic waves

Maxwell's equations describe the electromagnetic waves' propagation through matter and in vacuum [18]:

$$\vec{\nabla} \cdot \vec{D}(\vec{x},t) = \rho(\vec{x},t) \qquad \vec{\nabla} \cdot \vec{B}(\vec{x},t) = 0 \tag{1.1}$$

$$\vec{\nabla} \times \vec{E}(\vec{x},t) = -\frac{\partial}{\partial t}\vec{B}(\vec{x},t) \qquad \vec{\nabla} \times \vec{H}(\vec{x},t) = \vec{j}(\vec{x},t) + \frac{\partial}{\partial t}\vec{D}(\vec{x},t) \tag{1.2}$$

$\vec{E}(\vec{x},t)$ represents the electric field strength and $\vec{D}(\vec{x},t)$ is the electric displacement field. Furthermore, $\vec{H}(\vec{x},t)$ stands for the magnetic field strength, $\vec{B}(\vec{x},t)$ for the magnetic flux density. The charge density and the current density are represented by $\rho(\vec{x},t)$ and $\vec{j}(\vec{x},t)$, respectively.

In an isotropic medium the following relationships hold:

$$\vec{B}(\vec{x},t) = \mu_r \vec{H}(\vec{x},t) \ , \tag{1.3}$$

$$\vec{D}(\vec{x},t) = \epsilon_r \vec{E}(\vec{x},t) \ , \tag{1.4}$$

where μ_r is the material's permeability and ϵ_r is its relative permittivity. Assuming that there are no sources and currents, the wave propagation can be written as the wave equations of its electrical and magnetic constituents [18]:

$$\left(\vec{\nabla}^2 - \epsilon_r \mu_r \frac{\partial^2}{\partial t^2}\right) \vec{E}(\vec{x},t) = 0 \tag{1.5}$$

$$\left(\vec{\nabla}^2 - \epsilon_r \mu_r \frac{\partial^2}{\partial t^2}\right) \vec{B}(\vec{x},t) = 0 \ . \tag{1.6}$$

Equation (1.5) can be solved by

$$\vec{E}(\vec{x},t) = E_0 \cdot e^{i(\vec{k}\vec{r}-\omega t)} \ , \tag{1.7}$$

which includes the wave vector $\vec{k}$ and the angular frequency ω [18]. Making use of the dispersion relation $(\vec{k})^2 = {}^{\omega^2}/_{c^2}$ that sets $\vec{k}$ in relation with the angular frequency, and considering propagation through material with μ_r, ϵ_r, the following expression for the wave vector holds:

$$|\vec{k}| = n\frac{\omega}{c} \ , \tag{1.8}$$

where

$$n = \sqrt{\mu_r \epsilon_r} \tag{1.9}$$

is the refractive index.

1.1.2 Interaction with matter

Each material has a specific relative permittivity ϵ_r and permeability μ_r that account for the interaction of electromagnetic waves with the material. The refractive index $n = \sqrt{\epsilon_r \mu_r}$ of a material combines these material-specific values. It can also be written as a complex quantity

$$n = 1 - \delta + i\beta \ . \tag{1.10}$$

In this formula, δ and β describe the material specific behaviour of phase shift and attenuation, respectively.
When passing through a medium, the intensity of the electromagnetic wave decreases along the path z with increasing thickness of the object. This is described mathematically by the Lambert-Beer law:

$$I(d) = I_0 \cdot e^{-\int_0^L \mu(z)\,\mathrm{d}z} \ , \tag{1.11}$$

where I_0 is the wave's initial intensity, $\mu(z)$ is the linear extinction coefficient that depends on the position in the object and L stands for the thickness of the material.
The interaction with matter also depends on the energy of the waves. In the regime of X-ray wave-lengths, the dominating matter-interaction effects are the photo-electric effect and Compton scattering (see figure 1.1) [19]. These two effects are explained in more detail in the following.

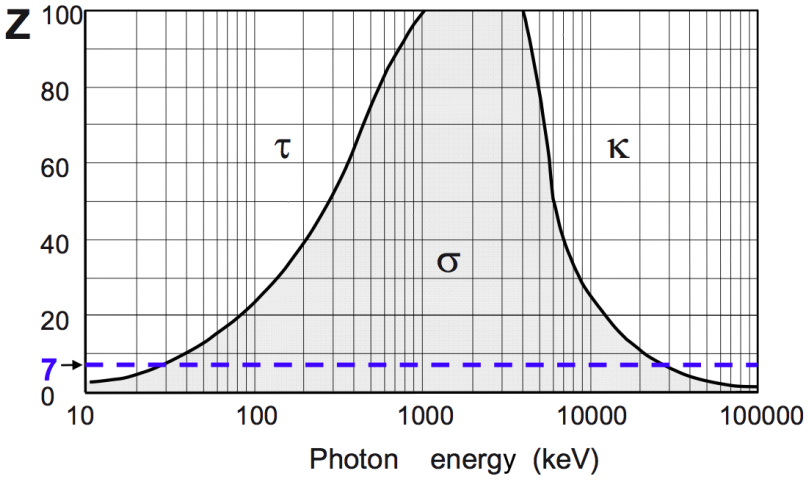

Figure 1.1: Overview of the regimes in which the different interaction mechanisms dominate. For X-rays (10 - 100 keV) and in biological tissue (blue dotted line, $Z \approx 7$), the photo-electric effect denoted by τ is prevalent. Towards higher photon energies, Compton scattering σ contributes more. Pair production κ cannot occur at all for energies lower than 1 MeV and thus is not relevant for medical imaging purposes. The solid lines indicate the areas where bordering processes have the same probability of occurring. Figure taken from [19].

1.1.2.1 Photo-electric effect

In the process that is called the photo-electric effect, a photon interacts with an electron in the shell of an atom. If its energy is higher than the electron's binding energy, the photon can separate the electron from the atom by being absorbed. The electron's kinetic energy E_{kin} is then given by

$$E_{\text{kin}} = E_{\text{photon}} - E_{\text{BE}} - E_{\text{recoil}} \ , \tag{1.12}$$

where E_{photon} is the incoming photon's energy, E_{BE} is the binding energy of the electron and E_{recoil} is the recoil energy. The latter can be neglected because of the big mass difference between electron and nucleus. The produced electron-hole in an inner shell is filled by an electron from an outer shell, producing a fluorescence photon or Auger-electron emission (see figure 1.2) [19].
The probability for the photo-electric effect is given by the photon absorption coefficient τ) [19]:

$$\tau \propto \rho \cdot Z^{3-3.5} \ . \tag{1.13}$$

For photon energies below 511 keV and above the K-edge of the absorber, τ decreases with E^{-3}. This behaviour is shown in figure 1.3. The cross section of the photo-electric effect σ_{ph} depends on the photon energy and on the atomic number of the atom it interacts with [18]:

$$\sigma_{\text{ph}} \propto \frac{Z^5}{E^{3.5}} \ . \tag{1.14}$$

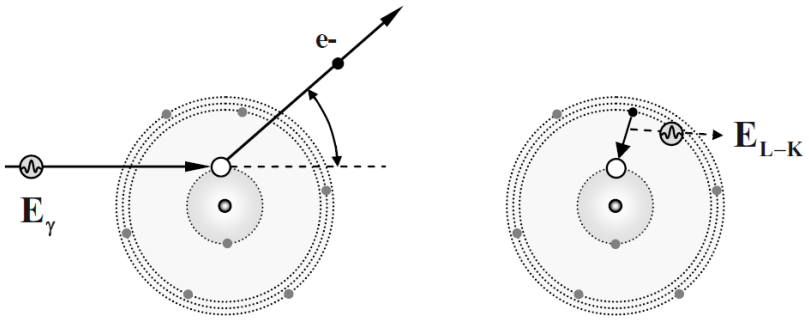

Figure 1.2: Illustration of the photo-electric effect with a K-electron. Left: Absorption of the photon by an electron in the K-shell, production of an electron hole. Right: An electron from the L-shell fills the hole, the energy difference is emitted as a photon. Figure taken from [19].

1.1.2.2 Compton scattering

The second dominating photon - matter interaction effect for X-rays is Compton scattering. It consists of inelastic interaction between the incoming photon and a quasi-free electron of the outer shells of the absorbing material. The photon transfers part of its energy and momentum to the electron. The former is scattered, i.e. changes its direction, whereas the latter is ejected

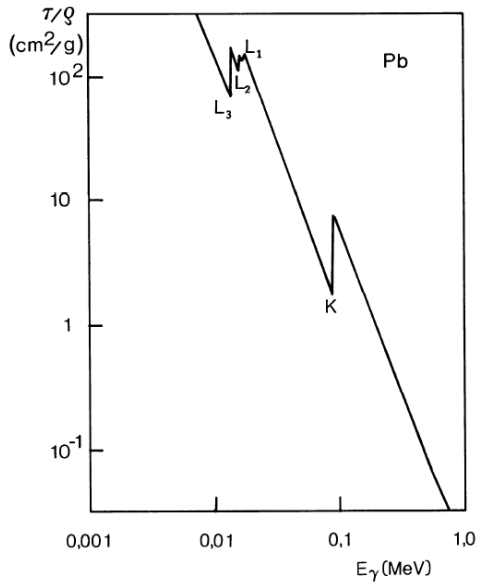

Figure 1.3: For lead, this graph shows the dependency of the photon mass absorption coefficient τ/ρ on the photon energy. L_{1-3} and K are the absorption edges for which the photon energy equals the binding energy of the respective electron shells and that are material specific. At the edges the absorption probability is at maximum, at neighbouring energies the mass absorption coefficient is smaller by almost an order of magnitude. Figure taken from [19].

from the atomic shell and leaves the atom ionised (see figure 1.4). The scattered photon must have a longer wavelength than the incident photon, as energy is transferred from the incident photon to the electron. Compton's formula for photon scattering from a stationary free or quasi-free electron is given by

$$\lambda_{\gamma,f} - \lambda_{\gamma,i} = 2\frac{h}{m_\mathrm{e}c}\sin^2\left(\frac{\theta}{2}\right) \ , \tag{1.15}$$

where $\lambda_{\gamma,f/i}$ are the final and initial wavelengths of the photon, m_e is the electron rest mass and θ is the deflection angle through which the photon is deflected from its initial direction [20]. This kind of interaction is also known as incoherent scattering. Compton was the first to interpret the process as inelastic scattering of two particles in 1923 [21].

The Compton interaction coefficient σ describes the probability of incoherent scattering. σ depends on the absorbing material's atomic number in relation to its mass number: $\sigma \propto \frac{Z}{A}$. As this ratio is 1/2 for most stable light elements except for hydrogen, one can say that Compton scattering is to a large extent independent of the absorbing element. It does, however, depend on the absorber's density ρ. For the energy dependency, there are several aspects that have to be taken into account. In an energy range from 0.2 to 10 MeV, it can be described empirically by the following expression:

$$\sigma \propto \rho \cdot \frac{Z}{A} \cdot \frac{1}{E_\gamma^n} \ , \tag{1.16}$$

where $n = 0.5 - 1$ [19].
To study the angular distribution and thereby the energy dependencies of Compton-scattered photons in detail, the Klein-Nishina formula from relativistic quantum mechanics is needed [20].

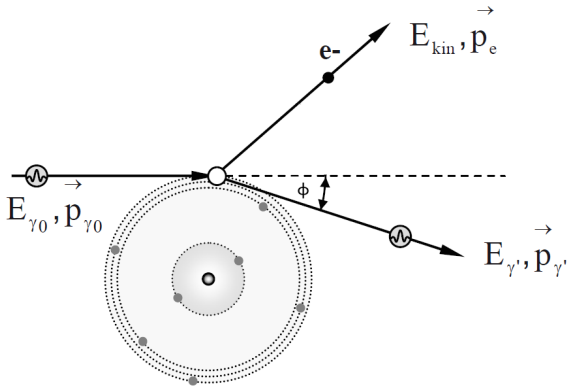

Figure 1.4: Compton scattering of the incoming photon with a weakly bounded electron. Depending on the scattering angle ϕ of the photon, the photon's energy and momentum are divided among the electron and the photon. Figure taken from [19].

1.1.3 Generation of X-rays

For medical imaging, X-ray tubes have been used to generate photons in the range of 10 - 150 keV since the discovery of this kind of radiation by Wilhelm Röntgen in 1895, which was published later in [22]. The main components of an X-ray tube are the cathode that produces thermal electrons, a high voltage acceleration of the electrons along an evacuated path and the anode material where the electrons' kinetic energy is converted into electromagnetic radiation. The physical processes occurring in the generation of X-rays are mainly Bremsstrahlung and characteristic radiation which will both be discussed in the following [23]. The overall spectrum of an X-ray tube is the sum of the contributions of both effects and depends on the acceleration voltage applied to the electrons.

1.1.3.1 Bremsstrahlung

The thermal electrons produced in the heated cathode are accelerated onto the anode. There, in the so-called target, the interaction between the electrons and the absorber material takes place [24]. When an electron is decelerated in the electric field of an atomic nucleus, Bremsstrahlung is produced. The attracting Coulomb forces deflect the electron that passes the nucleus' field. Forced onto a non-linear trajectory, the electron loses kinetic energy that is released as a photon. The energy loss is determined by the electron's initial energy, the nucleus' charge and the impact parameter (distance between nucleus and initial trajectory). As it is unlikely that the electron loses all its energy at once, the spectrum of produced photon energies is continuous. Usually, an electron undergoes several interactions, losing part of its energy in each. In order to increase the efficiency of the Bremsstrahlung production, X-ray tubes contain

targets of high density and high atomic numbers. The energy loss per distance is described by the following equation:

$$S_{\mathrm{rad}} = \frac{\mathrm{d}E}{\mathrm{d}x} \propto \rho \left(\frac{e}{m_{\mathrm{e}}}\right)^2 Z^2 E_{\mathrm{tot}} \ , \tag{1.17}$$

where Z is the atomic number, ρ the density of the target material, e/m_{e} the specific charge and E_{tot} the total energy of the incoming electron [24].

1.1.3.2 Characteristic radiation

The electrons that are emitted from the X-ray tube's cathode can also interact with the target's electrons. In a collision with a shell electron, the incoming electron can transfer more than the shell electron's binding energy onto the latter so that it is ejected from the shell. It is highly likely that in the ionized atom the hole in the inner shell is filled up again by an electron from a higher shell. The potential energy difference between the two shells is either released as electromagnetic radiation, the so-called characteristic radiation, or as an Auger electron. In case of characteristic radiation, the following equation holds:

$$E_{\mathrm{rad}} = E_n - E_m \ , \tag{1.18}$$

where E_{rad} is the energy of the produced photon and E_n, E_m are the energies of the outer and inner shell, respectively [25]. This type of radiation is called characteristic, as the energy difference between the shells and therefore the energy of the produced photons is characteristic for the element the anode is made of. The resulting spectrum is a discrete line spectrum [24]. As a prerequisite, the impinging electron's energy has to exceed the binding energy of the shell electrons for characteristic radiation to occur [23, 26].

1.2 Talbot-Lau Interferometry

1.2.1 Talbot effect

The Talbot effect can be observed in near-field diffraction [27]. When a periodic grating is placed in the path of a plane wave, the pattern of the grating is repeated at well-defined distances (Talbot lengths $n \cdot z_{\mathrm{T}}$, $n \in \mathbb{N}$) from the plane in which the grating is located. Lord Rayleigh calculated the theoretical Talbot distance to be

$$z_{\mathrm{T}} = \frac{\lambda}{1 - \sqrt{1 - \left(\frac{\lambda}{d}\right)^2}} \tag{1.19}$$

where d is the period of the grating and λ is the wavelength of the light [28]. For λ^2 small in comparison with d^2, the Talbot distance can be approximated by [29]

$$z_{\mathrm{T}} = \frac{2d^2}{\lambda} \ . \tag{1.20}$$

For one-dimensional phase gratings, there are fractional Talbot distances that occur with monochromatic parallel X-ray beams given by the following equation [30]

$$z_{\mathrm{f,1D}} = (2k-1)\frac{p_1^2}{2\lambda\eta^2} \ , \tag{1.21}$$

where p_1 is the period of the phase grating, and $\eta = 1$ for $\pi/2$-shifting gratings or $\eta = 2$ for π-shifting gratings [31]. The resulting pattern of images of the grating is called Talbot carpet (see figure 1.5) [29].

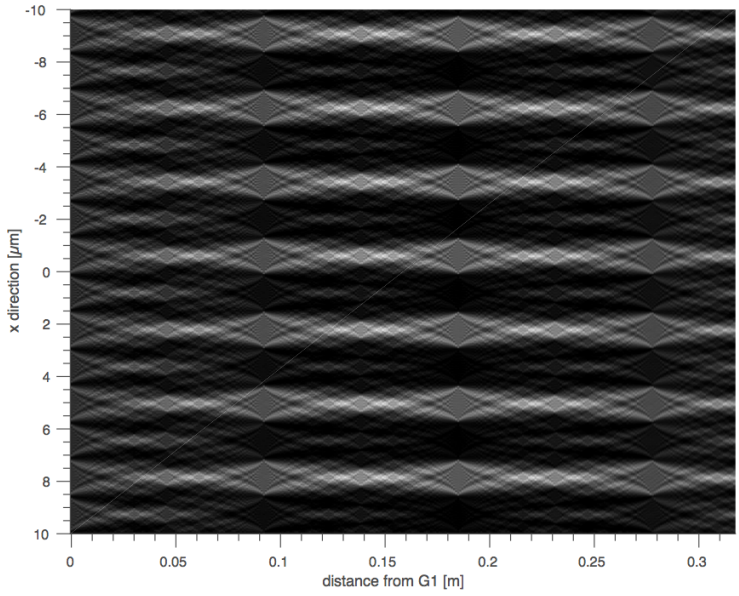

Figure 1.5: Simulated Talbot carpet for a plain wave. At 0.09 m distance from the first grating G1 (fractional Talbot distance) and at integral multiples of that number, self-images of the grating can be observed.

For a more detailed examination of the effect, the propagation of the wave front can be expressed in a simplified manner as a convolution of the wave function Ψ and the Fresnel propagator [20]:

$$\Psi(x, y, z + \Delta_z, t) = \Psi(x, y, z, t) * P_{\Delta_z}(x, y). \tag{1.22}$$

The Fresnel propagator in real-space is an operator representation of the Fresnel diffraction integral [20].

$$P_{\Delta_z}(x, y) = -\frac{ik\exp\left(ik\Delta_z\right)}{2\pi\Delta_z}\exp\left(\frac{ik(x^2+y^2)}{2\Delta_z}\right) \tag{1.23}$$

In momentum space the convolution corresponds to a multiplication of the Fourier transforms. By placing a 1-dimensional periodic grating in x-direction with period d in the beampath of the wave, specific wave vectors with $k_x = {}^{2\pi}/_{d} \cdot m$, with $m \in \mathbb{N}$ are selected. The resulting Fresnel propagator in momentum space is

$$\mathcal{F}(P_{\Delta_z})(k_x = \frac{2\pi m}{d}) = \exp\left(ik\Delta_z\right)\exp\left(\frac{-i\Delta_z 2\pi^2 m^2}{kd^2}\right) \ . \tag{1.24}$$

If the Fresnel propagator only produces a constant phase shift of $\exp(ik\Delta_z)$, then there is self-imaging of the grating structure. This is the case for the Talbot distance $\Delta_z = z_\mathrm{T} = {}^{2d^2}/_{\lambda}$ mentioned above (see equation (1.20)) [20].

1.2.2 Lau effect

The effect of self-imaging as observed with a grating and a plane wave is also possible for spatially incoherent and polychromatic light. For extended light sources without further modification of the set-up, there are extinction effects in the detection plane, which disturb the self-imaging. By placing an additional grating directly downstream of the source, each slit serves as a small light source that is coherent in itself and periodic images of the G1 grating are generated on the observation screen [32]. For appropriate choice of periodicity of the source grating, these self-images interfere constructively and a superposition of all self-images can be observed on the detector. This way, the light from the source is no longer required to be collimated or coherent [29].

1.2.3 Phase-contrast radiography

Making use of the aforementioned optical effects, the field of phase-contrast imaging has emerged. At first, the applications were exclusively in the regime of visible light. Then, in 1992, Clauser and Reinsch [9] theoretically predicted the possible applications of Talbot-Lau interferometry in the X-ray regime. However, phase shifts are very small for short wavelengths like in X-rays, and consequently are hard to measure. In addition to this obstacle, it is technically challenging to produce gratings that have suitable attenuation properties for application with X-rays. Therefore, it has taken some time until the technology could be applied in the regime of X-rays. As pioneers, Momose et al. [10] presented a novel method to use Talbot interferometry for phase-sensitive X-ray radiography in 2003 using two gratings of the same periodicity. The intensity pattern in the detector plane that is in the order of µm is evaluated in [10] via the Moiré fringes that result from tilting the second grating with respect to the first one. As the intensity pattern is usually much smaller than the size of a detector pixel, it cannot be resolved using only a pixelated detector. In 2005, Weitkamp et al. [11] resolved this issue by introducing the phase-stepping technology that makes X-ray phase-contrast imaging more suitable for practical purposes. Pfeiffer et al. [12] established the source grating as a further addition to the phase-contrast technology that allows applications with regular X-ray tubes that have an extended spot size, in contrast to synchrotron sources that are used in the previously mentioned approaches.

Figure 1.6 shows a schematic representation of the set-up that can be used with a regular X-ray tube and where the intensity pattern is analysed via phase-stepping. The analyser grating (G2), applied in addition to the modulation (G1) and the source grating (G0), allows sampling of the intensity pattern in the detector plane. The G2 is shifted laterally in x-direction in order to sample the intensity modulation of the pattern in several acquisitions. Ideally, it consists of fully absorbing grating bars and fully transmitting slits and has a period like that of

the intensity modulation. Now, the set-up can be used to measure three different images of the object – attenuation, differential phase shift and dark-field – which are described in the following.

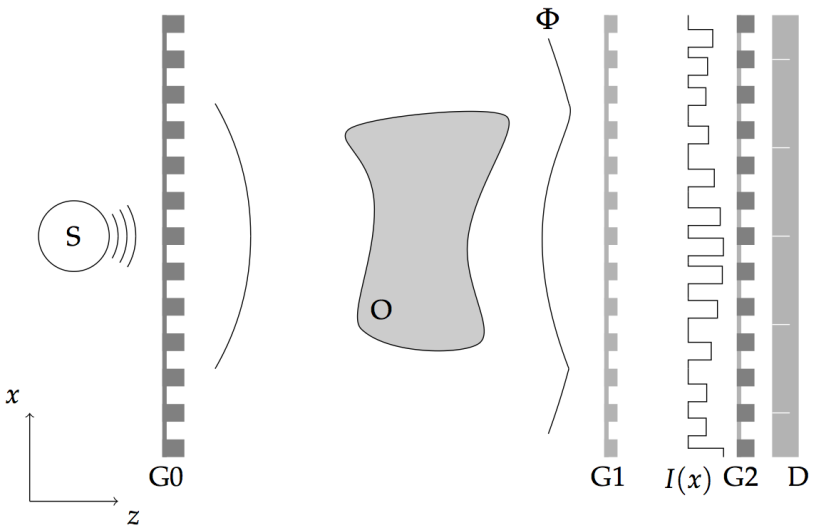

Figure 1.6: Representation of the Talbot-Lau interferometer that was used for the measurements in this thesis. The X-ray wave front Φ emitted by the source is split up into small coherent light sources by the source grating G0. The wave front is then distorted by the object O. At the Talbot distance downstream of G1, the intensity modulation pattern $I(x)$, which is a self-image of G1, is sampled by the analyser grating G2. The intensity is then measured using a pixelated detector D. Figure taken from [33].

The different images are calculated from the phase-stepping curve that results from sampling the intensity pattern with the analyser grating. For mono-energetic radiation at the design energy, a triangle function of the intensity is expected as a function of the G2 position. In reality, the phase-stepping curve is a sinusoidal function due to blurring of the superimposed self-images of the polychromatic source and the finite size of the G0 slits, among other reasons [33]. A schematic depiction of the resulting phase-stepping curve is given in figure 1.7.

Attenuation image The attenuation image is calculated as the quotient of intensity with and without the object in the path of the light, like in conventional X-ray imaging. In the phase-stepping curve, this information corresponds to the offset of the intensity signal.

$$\bar{\mu} = -\ln\left(\frac{I_{\mathrm{obj}}}{I_{\mathrm{ref}}}\right) = \int_0^L \mu(z)\,\mathrm{d}z \tag{1.25}$$

In this equation, $\bar{\mu}$ stands for the measured projection value in attenuation contrast. In projective imaging, $\bar{\mu}$ is the result of an integration of the local attenuation coefficients $\mu(z)$ over the length L of the object [17].

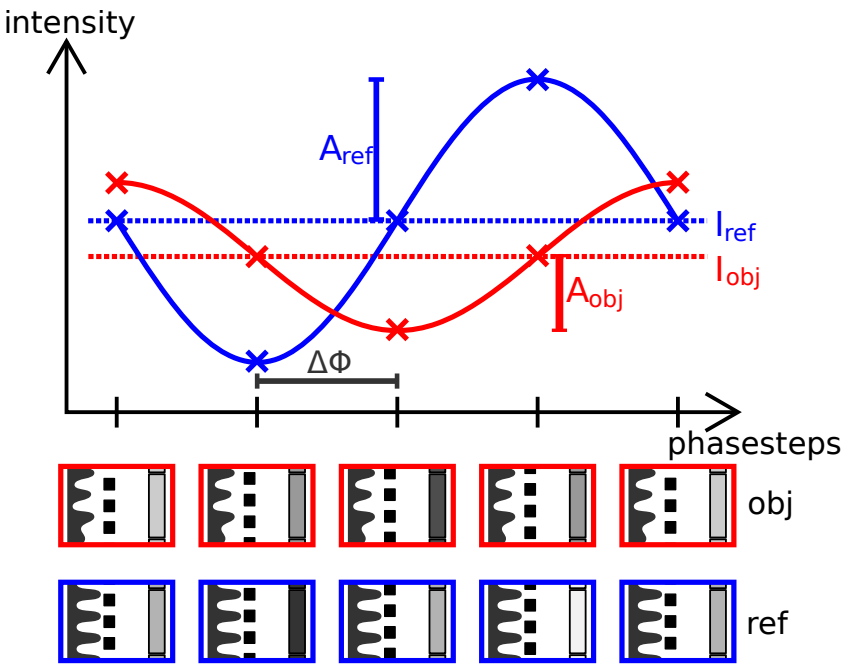

Figure 1.7: Phase-stepping curve that results from sampling the intensity modulation pattern by laterally shifting G2. The bottom figures show the corresponding intensity pattern for each position of the G2 (phase-step) (upper row: with object, lower row: reference). The brightness of the detector pixel on the right edge of the small figures visualises the intensity that is transmitted onto the detector pixel for each G2 position. The blue line in the upper figure indicates the reference measurement without an object in the beampath. The red line is shifted in phase, amplitude and intensity because of the object. $A_{\mathrm{ref/obj}}$ is the amplitude of the sinusoidal function. The mean intensity $I_{\mathrm{ref/obj}}$ of both curves is indicated by the dotted lines. $\Delta\Phi$ denotes the phase by which the object curve is shifted in comparison to the reference measurement. These three parameters are used to calculate the attenuation, differential phase and dark-field image. Figure taken from [34].

Differential phase image The differential phase image can be obtained from the data by measuring the phase value $\Delta\Phi$ by which the phase-stepping curve of the object is shifted relatively to the reference curve. Under the assumption of the small angle approximation, the following set of equations enables the calculation of the differential phase image:

$$\alpha = \frac{\lambda}{2\pi}\frac{\partial\Phi(x)}{\partial x} \tag{1.26}$$

$$d_\Phi(x) = \tan(\alpha) z_T = \frac{\lambda}{2\pi}\frac{\partial\Phi(x)}{\partial x} z_T \ . \tag{1.27}$$

α denotes the refraction angle by which the beam is deflected upon transmission through the phase-shifting object [12]. For X-rays, the deviation typically lies in the order of 10^{-6} rad, which justifies the small angle approximation. z_T is the distance between G1 and G2. d_Φ (see equation (1.27)) stands for the distance by which the intensity pattern is shifted laterally in the detector plane and that is measured in Talbot-Lau interferometry. It is the projection of the

phase shift $\Delta\Phi$. The differential phase shift of the wave front is denoted by $\partial\Phi(x)/\partial x$. From these observables the total phase shift of an object can be obtained by a one-dimensional integration along x:

$$\int_S \delta(x,s)\,\mathrm{d}s = -\frac{\lambda}{2\pi}\int_X \frac{\partial\Phi(x)}{\partial x}\,\mathrm{d}x \tag{1.28}$$

The path S connects the source with the point where the wave is detected [35].

Dark-field image Objects of the size of about 10^2 to 10^6 times the wavelength of the X-rays in the hard regime cause coherent scattering of X-ray photons. As a consequence, in a small cone around the direction of the incoming ray, the intensity is reduced compared to the unperturbed intensity measured without an object (small-angle scattering) [36]. The image that is produced considering these effects is called dark-field image. Its calculation is based on the visibility V that can also be used to describe the quality of a Talbot-Lau interferometry set-up. The visibility is defined as

$$V = \frac{A}{I}\ , \tag{1.29}$$

where A and I are the corresponding parameters from the phase-stepping curve. Using these quantities, the dark-field image is calculated as:

$$D = \frac{V_{\mathrm{obj}}}{V_{\mathrm{ref}}}\ . \tag{1.30}$$

From the aforementioned equations it can be understood that a change in amplitude of the interference pattern results in a dark-field signal. Thus, when the object causes coherent scattering in addition to the Talbot pattern, a dark-field signal is produced. Therefore, the dark-field image can be regarded as a measure of the scattering potential of an object. A measure of that property is the linear diffusion coefficient ϵ that quantifies the scattering per unit length. It is derived from the dark-field signal under the simplified assumption of ideally random scattering as follows:

$$\bar{\epsilon} = -\ln D = i\int_0^L \epsilon(z)\mathrm{d}z\ . \tag{1.31}$$

L stands for the object thickness, $\bar{\epsilon}$ is the resulting mean linear diffusion coefficient from the integration over the local coefficients $\epsilon(z)$ and i is a set-up specific constant [37].

Chapter 2

Materials and Methods

Contents

The following chapter comprises the technical parameters of the set-ups used for measurements in this thesis. In addition, the concepts of Dual Energy radiography and Computed Tomography (CT) are presented. These two methods were used to obtain data that makes more sophisticated evaluation possible. Finally, the algorithm is explained with which the material differentiation of Dual Energy CT data was carried out.

2.1 Talbot Lau Interferometer

There are two Talbot Lau interferometry set-ups used for the measurements presented in this thesis, one for CT measurements and one for obtaining projective images. Both set-ups have different gratings and distances between the components. Both follow the principle presented in section 1.2.3 and are presented shortly with their respective parameters.

2.1.1 Projective set-up

The projective images in this thesis were obtained using a set-up that is built vertically with the source on the ground and gratings and detector above it. A picture of the Talbot Lau interferometer is shown in figure 2.1. The X-ray tube that was used is a Siemens Megalix CatPlus 125/40/90 with a focus size of 0.4 mm (IEC 60336) and a range of 40 - 125 kV peak acceleration voltage. The grating parameters are listed in table 2.1.

Table 2.1: Grating parameters for the projective set-up

	Period	Duty cycle	Height
G0	24.39 µm	0.5	180 µm
G1	4.37 µm	0.76	6.4 µm
G2	2.4 µm	0.5	100 µm

The G0 and G2 have a duty cycle of 0.5, i. e. slits and grating bars have the same width. They both are absorption gratings, whereas G1 is a phase grating which causes a π-shift at 31.8 keV. The distance from the focus to G0 is 230 mm, from G0 to G1 1330 mm, from G1 to G2 130 mm and the detector is placed 230 mm downstream of G2. The detector model was an integrating detector Shad-o-Box 6K HS by Teledyne Dalsa with a pixel size of $49.5 \times 49.5\,\mu m^2$. The object was placed at 460 mm in front of the detector, yielding a magnification factor of $M = 1.33$ in the dectector plane.

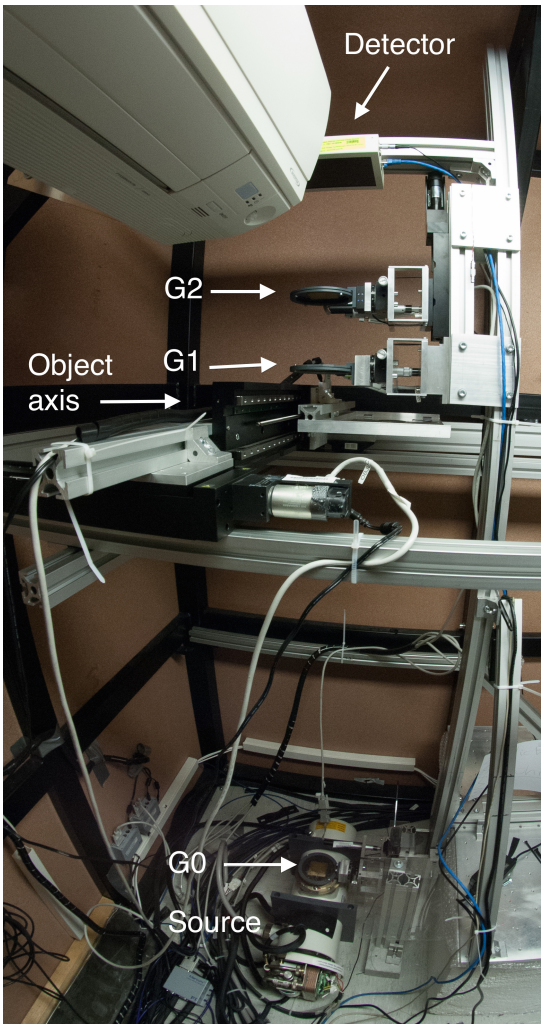

Figure 2.1: Picture of the experimental set-up used for projective measurements. The components are labeled, from top to bottom: Shad-o-Box 6K HS detector, G2, G1, object axis that is used to move bigger objects transversally through the set-up's field of view, G0 and X-ray source Siemens MEGALIX CatPlus.

2.1.2 CT set-up

The CT set-up is placed horizontally on an optical table. A disk is mounted o the table between G1 and G0. Thus, the object can be placed on this disk and and can be rotated around its axis vertically to the beampath. In addition to that, it can also be moved laterally in and out of the beam path. A picture of this set-up is shown in figure 2.2. Two different sets of gratings were used during the measurements, one for the plastic rods and kidney stones and another one for the ribs. The grating parameters are listed in table 2.2.

Table 2.2: Grating parameters used for measuring different objects in the CT set-up. The asterisk marks a bent grating.

Object	Grating	Period	Duty cycle	Height
Rib	G0	13.31 µm	0.5	$\geq$ 230 µm
	G1	5.71 µm	0.3	6.3 µm
	G2	10 µm	0.5	200 µm
Plastic rods, Kidney stones	G0	11.54 µm	0.5	290 µm
	G1	3.39 µm	0.5	6.37 µm
	G2	4.8 µm	0.5	180 µm*

All distances between the components of the set-up for the different measured objects are listed in table 2.3. Magnification varied for the different measurements as the objects were placed at different distances from the detector, the numbers are also given in table 2.3. The detector used in the CT set-up is a PaxScan 2520D by Varian Medical Systems with $127 \times 127\,\mu m^2$ pixel size. CT measurements were carried out using 0.3 mm of copper filtering in front of the source. The source is the same as in the projective set-up.

Table 2.3: Grating positions for the different measurements performed with the CT set-up.

Distances	Plastic rods	Plastic swarf	Rib	Kidney stones
Focus – G0	154 mm	154 mm	164 mm	173 mm
G0 – G1	973 mm	973 mm	685 mm	840 mm
G1 – G2	402 mm	402 mm	515 mm	350 mm
G2 – Detector	420 mm	420 mm	190 mm	197 mm
Magnification	2.2	1.8	2.2	1.8

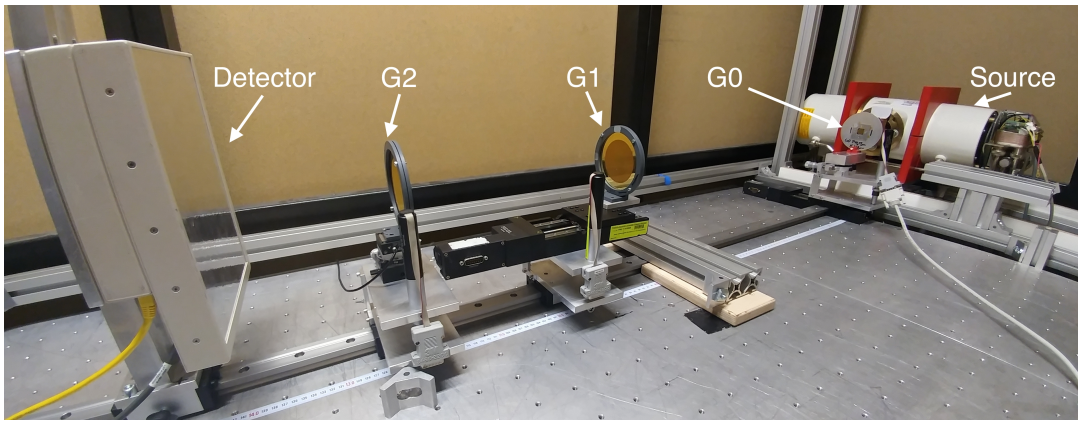

Figure 2.2: Picture of the experimental set-up used for CT measurements. Components from left to right: Varian PaxScan detector, G2, G1, G0, Siemens MEGALIX source with copper filtering. The object was placed in front of G1 on top of a rotational axis.

2.2 Dual Energy CT

Based on the physical fundamentals presented in chapter 1, two secondary methods are used to conduct experiments. Firstly, Dual Energy X-ray imaging, where ambiguities between two materials with the same attenuation coefficient μ at one energy can be resolved by measuring the object at different photon energies. Secondly, phase-contrast measurements were not only conducted projectively, but also as Computed Tomography. CT data have the advantage of holding the refractive index decrement instead of the differential phase that is obtained in projective measurements. In addition to that, the absolute attenuation and dark-field coefficients in each pixel are obtained in CT in contrast to the integrated quantities that result from a projective measurement. Both concepts are presented shortly.

2.2.1 Dual Energy X-ray

In conventional X-ray radiography, the Dual Energy method is mainly used to examine the bone density of patients with osteoporosis [4]. Carrying out X-ray measurements at only one photon energy can lead to ambiguities, as the attenuation depends on atomic number and density of the material. At certain combinations of these physical quantities, the resulting μ can be identical for different materials. Making use of the fact that X-ray attenuation also depends on the energy of the photon, measuring the transmission at two different peak acceleration voltages, and thereby at different photon energies, allows the calculation of the areal densities (mass per projected area) of two different materials [38]. As a prerequisite for the Dual Energy method, the polychromatic spectra $w(E)$ at the two acceleration voltages or rather maximum photon energies E_1, E_2 have to be different from each other:

$$w(E_1) \neq w(E_2)$$

In principle, this method builds on the fact, that the attenuation coefficient $\mu(\vec{r}, E)$ at a certain point in space $\vec{r}$ and energy E can be split into contributions by the photo-electric effect and

those by the Compton effect in the energy range of X-rays (compare figure 1.1) [39]:

$$\mu(\vec{r}, E) = \tau_0(\vec{r})\tau(E) + \sigma_0(\vec{r})\sigma(E) \tag{2.1}$$

Physically, the maximum number of base functions is 2, as both interaction effects depend on two characteristics of the material: its density ρ and its electron density that depends on the atomic number Z (see equation (1.14) and equation (1.16)). These base functions, however, do not have to be photo-effect and Compton scattering or ρ and Z but can be any known energy dependencies $\Psi_1(E)$ and $\Psi_2(E)$ with unknown spatial coefficients $f_1(\vec{r})$ and $f_2(\vec{r})$. In clinical practice, a contrast agent like iodine, xenon or barium is often used to differentiate two tissues more precisely [1]. These elements are particularly well-suited for the task, as they have atomic numbers around $Z = 55$. At low energies, the photo-effect dominates at that atomic number because of interaction with the inner K shell. Most atoms in body tissues (hydrogen, carbon, nitrogen, oxygen) on the other hand have low atomic numbers and therefore a rather low attenuation by photo-electric effect. Therefore, there is strong spectral contrast between contrast agents and soft tissue which is taken advantage of in angiography, for example [1]. By adding information obtained through phase-contrast imaging, no additional material can be differentiated, because the phase shift also depends on the material's electron density, but the two materials can be identified more precisely.

Postprocessing of clinical Dual Energy CT data is regularly done using three main types of algorithms which either optimize the images, differentiate certain materials or quantify substances in the dataset [1]. The output of the latter two algorithms usually colour-code substances, which is why this visualisation was also employed in this thesis (see section 2.2.3).

2.2.2 Computed Tomography

The possibility to obtain 3D-images of a patient has been available since 1972, when the first head CT scanner was introduced [26]. Over the decades, CT scans and reconstruction have become faster and more technologically sophisticated. The groundwork for this medical imaging technology was laid in 1917 by Radon who developed the mathematical principles of Computed Tomography [40]. It was not until the 1970s that his work was rediscovered and its impact was appreciated. Radon proved that using an infinite number of projections through an unknown object, an image of it can be calculated. In practice, a finite but large number of X-ray images are acquired from different angles around the object and reconstructed into slices of CT images. Of course, a CT image is also a two-dimensional representation of a 3D structure. The slice thickness of each slice is determined by the voxel size and is usually very thin. In the set-up used in this thesis, the thickness of one slice lies in the order of 10^{-4} m. Consequently, CT images have a large advantage over projection images, as the path along which the image is integrated is much shorter, it is the voxel size instead of the object diametre.

2.2.2.1 Reconstruction method

The data acquired in a CT scan consists of a set of linear projections at different angles around the object. From each angle, one-dimensional projection data is obtained, as seen in figure 2.3a.

Displayed as line images, the projection data is stacked and fused into two-dimensional Radon transforms of the object that is called sinograms (see figure 2.3b). Along the vertical axis, the projection data in one detector row is displayed, on the x-axis variations over all projection angles are shown. An object that is not located in the rotational centre of the set-up will form a sinusoidal curve in the sinogram, hence the name of the image [41]. Starting from here, the most widely used reconstruction technique is called filtered backprojection (FBP), which in combination with a high-pass filtering on the projection signals is equivalent to Radon's solution [42]. Its working principle is to reverse the acquisition steps: the attenuation information that was integrated along the path of the X-ray beam by the detector is now smeared along the same path. Doing this for a number of different angles, areas of high attenuation reinforce each other. The original distribution of attenuation coefficients $f(x, y)$ is obtained by integrating the Fourier transform $P_\gamma(q)$ of the projection data $p_\gamma(\xi)$:

$$f(x,y) = \int_0^\pi \int_0^\infty P_\gamma(q) e^{2\pi i q \xi} \, |q| \, \mathrm{d}q \, \mathrm{d}\gamma \ . \tag{2.2}$$

Multiplication by $|q|$ indicates a high-pass filtering of the projection data, ensuring enhanced edges and evening out averaging along a ray [41]. Delevoping the approach in equation (2.2) further, the high-pass filter was complemented by Ramachandran and Lakshminarayanan with a rectangular function rect(q) that $|q|$ is multiplied by, in order to prevent high noise frequencies from being amplified [43]. In order for FBP to be applicable, the precise geometry (parallel beam, fan beam) of the data acquisition is required as well as complete projection data from 180° or 180° + α, with α the fan beam angle, around the object [26]. In the attenuation image, the CT scan gives Hounsfield units (HU) as a result of the calculation of the projection data $p_\gamma(x)$ from the intensity transmitted through the object $I(x)$ and from that in free field I_0 [26]:

$$p_\gamma(x) = \ln\left(\frac{I_0}{I(x)}\right) = \mu x \ . \tag{2.3}$$

The grey level of each pixel represents the numerical value of the average linear attenuation coefficient μ of the object contained in the voxel. Hounsfield units are normalized to the attenuation coefficient of water and multiplied by 1000 to ensure a range that can be displayed by computer hardware [26]:

$$\mathrm{HU} = 1000 \cdot \frac{\mu_{\mathrm{pixel}} - \mu_{\mathrm{water}}}{\mu_{\mathrm{water}}} \tag{2.4}$$

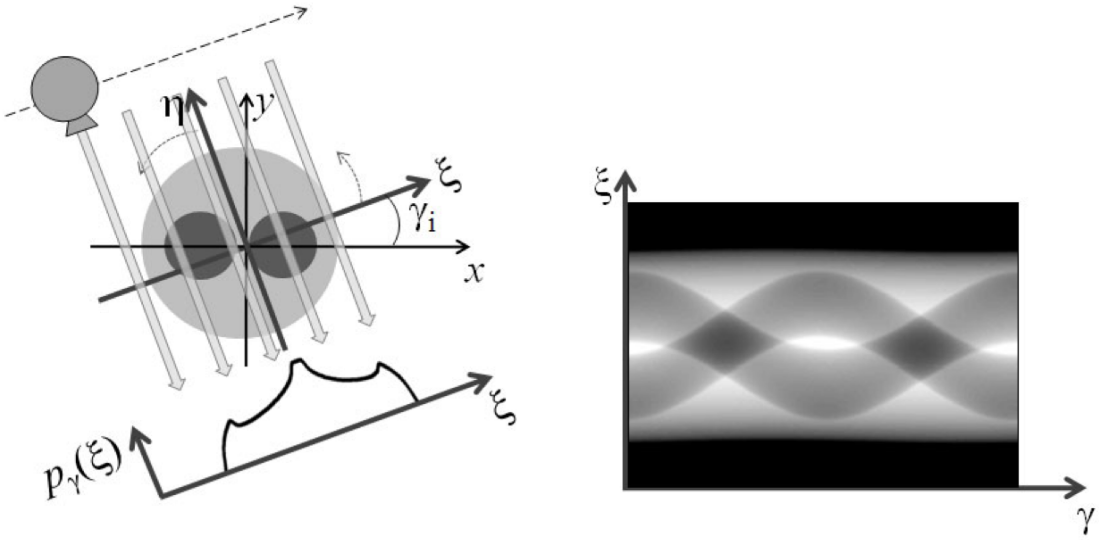

(a) Schematic depiction of the projection data $p_\gamma(\xi)$ that is obtained during a measurement at the angle γ with respect to the object coordinate system (x, y). The source is modelled as a parallel beam and rotates relatively to the object in the source-detector coordinate system (η, ξ).

(b) Resulting 2D sinogram combined from 1D projection measurements at angles $0° \leq \gamma \leq 360°$ along all positions ξ in one detector row. The result is the Radon transform of the object in parallel beam geometry.

Figure 2.3: The two images illustrate the first steps of CT imaging: **(a)** obtaining projection data of one layer in the object and **(b)** combining measurements from all angles of that layer to a sinogram. Figures taken from [41].

2.2.2.2 Ring artifacts

Artifacts that can be observed generally in most CT images are rings that are formed around the centre of the image, like for example in figure 2.4a where they lie concentrically around the centre of the uncropped imaged. Ring artifacts are present in most CT images due to the CT reconstruction. The artifacts are superimposed structures that can be caused by imperfect or defective detector elements that lead to an under- or overestimation of the attenuation coefficient [44]. For the removal of the ring artifacts from the data in the following two sections, an algorithm[1] is used that smears out the data from the centre to the edges, based on the algorithm introduced by Prell, Kyriakou, and Kalender in [44]. Firstly, the algorithm checks whether a pixel value in the original image lies within a pre-defined interval, and if so, the original value is kept in the threshold image f_T. All other pixel values are preliminarily set to zero in f_T. They are then set to the rounded value of the radially neighbouring pixels in a distance that can be chosen manually. For the data in this thesis, the distance value was set to the surrounding two pixels that lie inside of the same circular artifact R_A. The circular artifact

[1]The ring artifact removal algorithm was kindly provided by Sebastian Käppler, Pattern Recognition Lab, Friedrich-Alexander-Univerität Erlangen-Nürnberg.

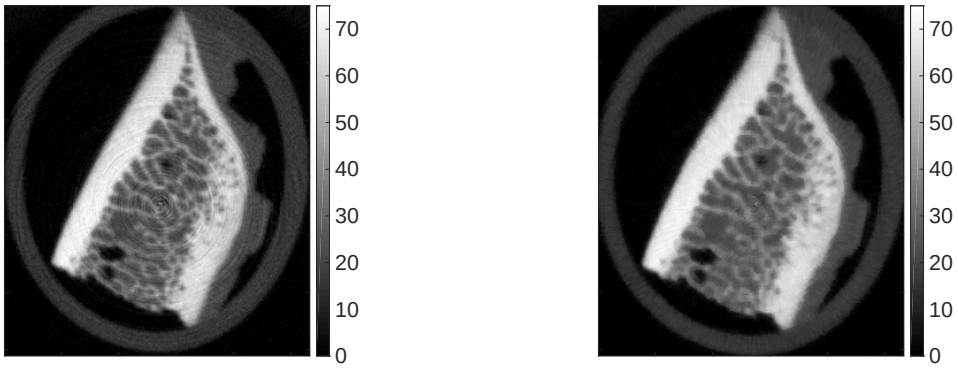

(a) Raw image **(b)** Image corrected for ring artifacts

Figure 2.4: Slice of an attenuation CT image (μ in m^{-1}) showing a porcine rib **(a)** with ring artifacts and **(b)** after correcting the artifacts with the algorithm described in the text.

size R_A is calculated as

$$R_\mathrm{A} = \frac{R_\mathrm{F}}{R_\mathrm{D} + R_\mathrm{F}} \cdot P_\mathrm{D} \cdot \frac{b}{P_\mathrm{I}} \ , \tag{2.5}$$

where R_F stands for the distance from the rotation axis to the focus, R_D denotes the distance form the rotation axis to the detector, P_D is the detector pixel size and P_I is the image pixel size that consists of detector pixel size divided by the magnification. b stands for the pixel binning factor that was equal to 1 in the set-up used. The resulting rounded values are saved in an image f_M. By adding the threshold image to the mean image, the final corrected image f_C is obtained:

$$f_\mathrm{C} = f_\mathrm{T} + f_\mathrm{M} \ . \tag{2.6}$$

An example for the resulting corrected image is shown in figure 2.4b.

2.2.3 Algorithm for pixelwise material allocation

In order to make use of Dual Energy CT images of objects, an algorithm was implemented that assigns each pixel in the image to a known material. This is possible with up to four different materials using the attenuation coefficient and refractive index decrement. Before evaluating the images, the materials have to be characterized by carrying out calibration measurements at the respective energies with identical spectra as in the measurements of the object that is to be allocated. Then, a system of linear equations is solved to determine proportions of the materials in each pixel:

$$\begin{aligned}
\mu_\mathrm{tot}(E_1) &= x_1 \cdot \mu_1(E_1) + x_2 \cdot \mu_2(E_1) + x_3 \cdot \mu_3(E_1) + x_4 \cdot \mu_4(E_1) \\
\mu_\mathrm{tot}(E_2) &= x_1 \cdot \mu_1(E_2) + x_2 \cdot \mu_2(E_2) + x_3 \cdot \mu_3(E_2) + x_4 \cdot \mu_4(E_2) \\
\delta_\mathrm{tot}(E_1) &= x_1 \cdot \delta_1(E_1) + x_2 \cdot \delta_2(E_1) + x_3 \cdot \delta_3(E_1) + x_4 \cdot \delta_4(E_1) \\
\delta_\mathrm{tot}(E_2) &= x_1 \cdot \delta_1(E_2) + x_2 \cdot \delta_2(E_2) + x_3 \cdot \delta_3(E_2) + x_4 \cdot \delta_4(E_2)
\end{aligned} \tag{2.7}$$

In the linear system, x_i are the volume proportions of the materials at the X-ray energies $E_{1/2}$. The total attenuation coefficient μ_{tot} and total refractive index decrement δ_{tot} in a pixel are composed of the respective contributions μ_i and δ_i of the four materials. The equations are solved for x_i under the boundary condition that $x_i \geq 0$. Finally, the image is re-plotted with a colour code using the biggest proportion in each pixel as an indicator for the material present. The results achieved using this method are presented in section 3.1.

Chapter 3

Results and Discussion

Contents

Projective and CT measurements of plastic objects like rods and swarf were carried out in order to test the allocation algorithm for Dual Energy measurements. The results were transferred onto measurements of a biological sample (porcine rib with muscle, fat and bone marrow). The CT images were corrected for ring artifacts using an algorithm that is presented shortly. Furthermore, renal stones were measured in water and Dual Energy analysis was conducted in order to differentiate mineral compositions. Finally, it is shown that using phase-contrast CT, Uric acid stones have higher contrast to water than using conventional CT methods.

3.1 Allocation of materials using Dual Energy CT

In this section, the results of Dual Energy phase-contrast CT (DEPC-CT) measurements are presented. Firstly, plastic rods were measured in the CT set-up (see section 2.1.2) and the material allocation algorithm (see section 2.2.3) was applied to the images. Secondly, the same procedure was carried out using porcine rib with muscle, fat and bone marrow as a biological sample.

3.1.1 Plastic rods

Three plastic rods made of Polytetrafluoroethylene (PTFE, $(C_2F_4)_n$), Polymethyl methacrylate (PMMA, $(C_5O_2H_8)_n$) and Polyvinyl chloride (PVC, $(C_2H_3Cl)_n$), each about 5 mm in diametre and 3 cm in length, were measured in the CT set-up using the gratings and distances listed in table 2.2 and table 2.3. A picture of the samples is shown in figure 3.1. The tube was set to ten different acceleration voltages and currents in order to have a variety of settings to choose from for the Dual Energy evaluation. The used settings are listed in table 3.1.

Table 3.1: Tube settings for plastic rod CT measurements.

Peak acceleration voltage [kV]	55	60	65	70	75	90	100	110	120
Current [mA]	32	21	15	10	7	3	2	2	2

An exemplary set of CT images is shown in figure 3.2. As the plastic is homogeneous, scattering only occurs at the edges of the rods and the dark-field image is not meaningful. Thus, the dark-field CT slice is omitted here. The images obtained by CT measurements are quantitative with respect to the used spectrum with its effective energy, i.e. the value in each

Figure 3.1: Picture of the three plastic rods made of PTFE, PVC, PMMA. The rods are about $\varnothing = 5$ mm in diametre and about 3 cm in length.

pixel represents the material's attenuation coefficient or refractive index decrement, respectively. In order to give values in units of m^{-1}, the pixel values in the attenuation and dark-field image have to be corrected for set-up geometry by the factor c:

$$c = \frac{M}{x} = \frac{M}{127 \cdot 10^{-6}\,\mathrm{m}} \ , \tag{3.1}$$

where c depends on the magnification M given by the object position in the set-up and on the pixel size x that accounts for the voxel depth. The magnifications for the different measurements are listed in table 2.3. Using the correction, the attenuation coefficient μ and the dark-field coefficient ϵ are obtained independently from the set-up geometry in units of m^{-1}.
For the phase image, the pixel value has to be multiplied by a factor a in order to represent the refractive index decrement δ. The factor is defined as follows:

$$a = \frac{p_2}{2\pi z_T} = \frac{4.8 \cdot 10^{-6}\,\mathrm{m}}{2\pi \cdot z_T} \ . \tag{3.2}$$

The factor a is made up of the G2 period p_2 and the Talbot distance z_T of the set-up. The refractive index decrement δ depends on the refraction angle α in the following way:

$$\alpha(x) = \int_0^L \frac{\partial \delta(x,y)}{\partial x}\,\mathrm{d}y \ , \tag{3.3}$$

where L is the diametre of the object.

All values in the regions of interest (ROI) indicated by the rectangles in figure 3.2a were evaluated to obtain calibration curves of the three materials at each spectrum that was used. In the calibration curves, the mean of the ROI for each imaging modality is plotted over the peak acceleration voltage using the standard error of the ROI as errorbars. The resulting plots for attenuation, phase and dark-field image are shown in figure 3.3. The dashed lines are fit curves with the expected theoretical dependence, which is $\propto E^{-4}$ for the attenuation coefficient and $\propto E^{-2}$ for the refractive index decrement. The standard error of the data is negligible, as the number of pixels considered was in the order of 10^7. Therefore, the errorbars in the calibration curves are not discernible. The colored bands indicate the standard deviation of all the pixel values. It can be seen that for the attenuation values, the bands are distinguishable over the whole energy range, while the values of PTFE and PVC come closer to each other for higher energies. Looking at the refractive index decrements in figure 3.3b, it becomes apparent that although the mean values over all pixels differ for PVC and PMMA, one pixel cannot be allocated unambiguously to one of the two materials considering the standard deviation. For the dark-field coefficients, PTFE and PMMA have values close to zero, whereas PVC causes a larger dark-field signal. However, there is no unambiguous trend for ϵ over the acceleration voltage and more importantly, the bands of the standard deviations overlap for all three materials. This is why, for the material allocation algorithm, only the attenuation coefficient and refractive index decrement were considered. Following the method described in detail in section 2.2.3 the linear system is solved in each pixel for data obtained at 55 kV and 90 kV peak acceleration voltage. The linear system (see equation (2.7)) contains four equations, so that the system is overdetermined. The result is a colour-coded image that in each pixel displays the material

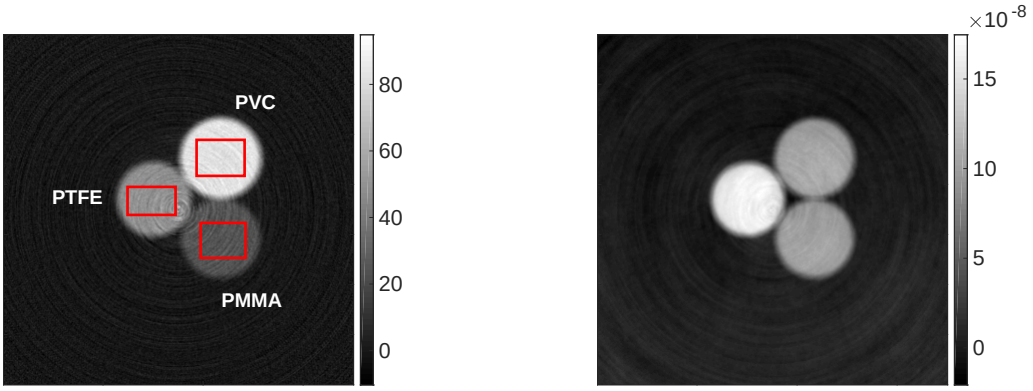

(a) Attenuation coefficient μ in m^{-1} **(b)** Refractive index decrement δ

Figure 3.2: One slice of the CT images of plastic rods (PMMA, PTFE, PVC) obtained at 55 kVp and 32 mA. The set-up used for this measurement is presented in section 2.1.2. In the attenuation image **(a)**, ROIs that are used to determine the mean value of each material for the calibration curves are indicated by rectangles. The same ROIs have been used for the other imaging domains.

with the highest proportion in the pixel. For pixels with $\mu \leq 10\,\mathrm{m}^{-1}$, the colour is set to white, as they do not contain the object but air. Furthermore, the result is averaged over all layers of the object, guaranteeing a more precise allocation. The result is shown in figure 3.4a, where it becomes apparent that the algorithm works well in general with slight drawbacks in the edge region of the object. Using only the data from one slice was not accurate, which is shown in figure 3.4b in comparison. This result poses a problem for application of the method on biological objects, as they are not translational invariant in any direction, which would be needed for averaging over several slices. The calibration measurements confirm that material information from only one slice cannot suffice, because only the mean values for PVC and PMMA are distinguishable, whereas for one pixel, the standard deviations overlap for both materials.

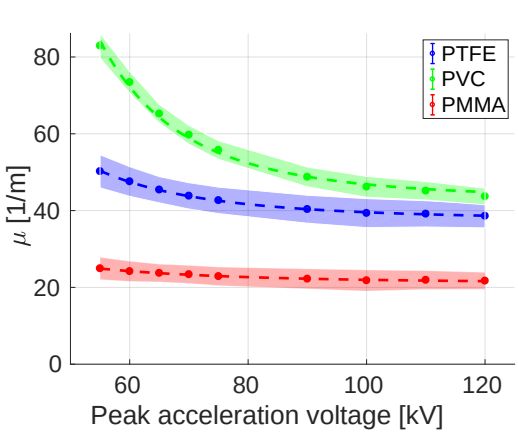

(a) Attenuation coefficient μ

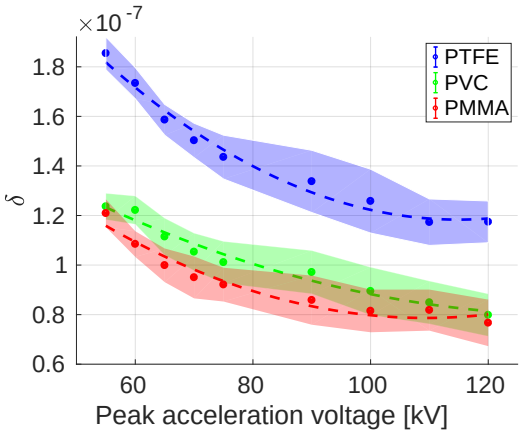

(b) Refractive index decrement δ

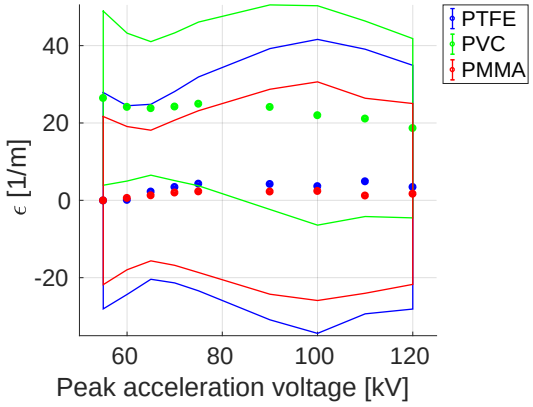

(c) Dark-field coefficient ϵ

Figure 3.3: Calibration curves for PMMA, PVC and PTFE measured at different peak acceleration voltages. The plotted material values are mean values of the ROIs shown in figure 3.2a, the dashed curves are fit curves, $\propto E^{-4}$ and $\propto E^{-2}$ for attenuation coefficient and refractive index decrement, respectively. The shaded areas indicate the band of one standard deviation around the data points. For the dark-field coefficient, only the outlines of the bands are shown for clarity.

(a) Average over all slices of the object. **(b)** One slice.

Figure 3.4: Result of the allocation algorithm (a) averaged over all slices and (b) of just one slice. For the latter, there is no clear differentiation possible between PTFE (left) and PMMA (bottom right). The allocated materials are colour-coded as follows: red = PMMA, blue = PTFE, green = PVC.

3.1.2 Plastic swarf

With regard to testing the allocation algorithm on a more challenging object, a sample is manufactured from swarf of the three plastic materials from the previous section. The pieces are mixed and put into a plastic syringe (see figure 3.5). Then they are compressed and measured in the same set-up as the rods with a resulting magnification of $M = 1.8$ (see table 2.3). The pixel allocation algorithm is applied to all sclices of the CT data in order to find the proportion of the materials in the mixture. It is based on the linear system containing four equations (see equation (2.7)) with the material properties at 60 keV and 90 keV in phase and attenuation, hence the system is overdetermined. All gauge values remain the same as in the previous section, as the swarf is made from identical plastic material as the rods.

A slice from the CT image of the object is shown in figure 3.6 alongside a projective picture where the position of the slice is indicated by a red line. The allocated picture that corresponds to the CT slice is shown in figure 3.7. In figure 3.7a, the allocated image for raw data is shown and in figure 3.7b that data which is corrected for ring artifacts using the method described above. From the algorithm's material allocation, volume proportions of the different materials in the whole object are calculated and listed in table 3.2. In order to assess the accuracy of the results, volume proportions are also calculated from the mass of each material in the object. The mass is measured using a scale with 10^{-4} g precision. From that quantity, the volume of each material is calculated and the results are listed alongside the algorithm's results in table 3.2. The range given for these numbers in the table originates from the range in density of the materials, which is not known precisely.

Before applying the allocation algorithm to the images, the syringe was cut from the image in order to only consider the three materials of the swarf and not the syringe material. Applying

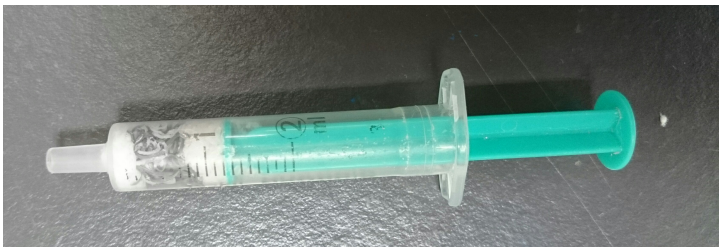

Figure 3.5: Picture of the swarf from the three plastic rods made of PTFE, PVC, PMMA compressed in a plastic syringe. The object is $\varnothing = 12\,\text{mm}$ in diametre and about 5 cm in length.

Table 3.2: Proportions of the three materials mixed as swarf in the object.

Material	Measured volume proportion	Allocated volume proportion	
		Raw data	Ring artifact corrected data
PMMA	29.3 - 32.6 %	35.5 %	37.3 %
PTFE	32.2 - 35.9 %	50.0 %	30.1 %
PVC	31.5 - 38.6 %	14.5 %	32.6 %

the allocation algorithm to the raw data yields results that agree with the volume proportions calculated from the mass less than the percentages obtained by using ring artifact corrected images. For the corrected images, only for PVC the volume proportions obtained with the algorithm lie in the range of the measured proportions, while the proportion of PMMA is overestimated and therefore that of PTFE is underestimated. Comparing the results, it has to be considered, that the weight measurements can also be flawed and therefore the ground truth for the volume proportions is unknown.

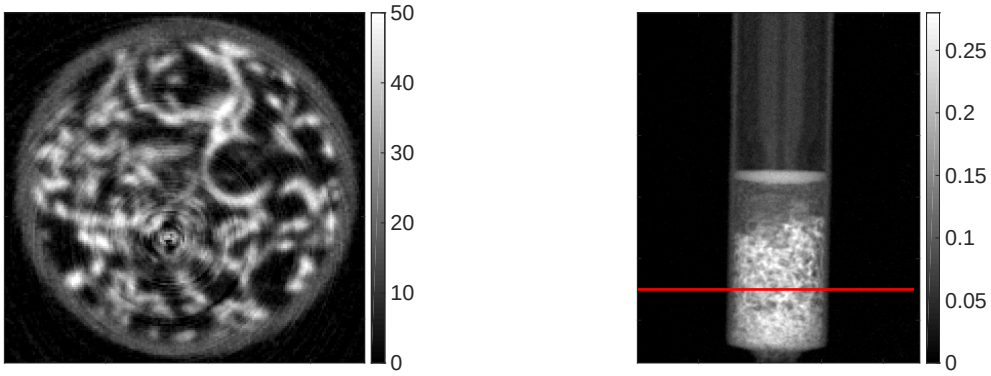

(a) Attenuation coefficient μ in m^{-1} in a slice of the CT image

(b) Projective attenuation image.

Figure 3.6: Attenuation images of the plastic swarf object. In (a) a CT slice of the object is shown, located where the red line in (b) indicates. In (b), the projective image is shown. Both images were obtained at 60 kV peak acceleration voltage and 21 mA current.

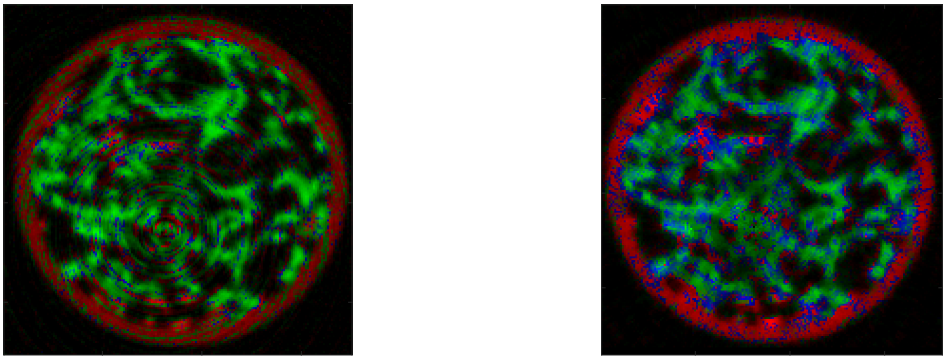

(a) Raw data.

(b) Data corrected for ring artifacts.

Figure 3.7: Results of the allocation algorithm for the plastic swarf object shown for the same slice as in figure 3.6a. The colour-code is the same as in figure 3.4. The calibration values used in the algorithm were obtained at peak energies of 60 keV and 90 keV.

3.1.3 Porcine rib

In order to examine the applicability of the allocation algorithm in a medical context, a porcine rib with bone marrow, muscle and fat was measured in DEPC-CT. In clinical practice, Dual Energy X-ray absorptiometry (DXA) is conducted in order to calculate body fat percentages. With regular radiography, however, this method is constrained to differentiating only two materials and the human body has to be considered as a two-component system [6]. Mostly,

only fat and lean soft tissue (consisting of water, proteins, glycogen and minerals [7]) are in the beampath. In the cases where there is bone in the beampath, surrounding regions are used to extrapolate the fat to muscle ratio and thus to estimate the body composition [5]. The underlying algorithm in DXA systems therefore solves a linear system for two components in each pixel, either fat and lean soft tissue or soft tissue and bone minerals [8]. This restricts the accuracy of body composition in projective X-ray radiography, as pixels containing bone mineral make up about one third of whole-body scans [6]. The assumption that the amount of fat near the bone is the same as that in the neighbouring soft-tissue region is not accurate, as adipose tissue in the abdomen can be distributed non-uniformly. In addition to that, the percentage of pure soft-tissue pixels is low in regions such as the thorax, arm and head, which further increases the difficulty for soft-tissue determination. Using phase-contrast methods, it is expected that the composition of an object can be determined more accurately. On the other hand, it has to be considered that the DXA technique only requires doses lower than 7 µSv [6], whereas the dose increases significantly when performing a CT scan of the whole body. A thorax scan in CT causes about 10 mSv of dose on the patient [19].

For the calibration measurements in this thesis, the main tissue types (fat, bone, muscle) of the rib sample are separated and measured each in the CT set-up whose technical details are described in section 2.1.2. Only the bone marrow is not removed from the bone but they are measured at the same time. Consequently, the bone marrow value is extracted from the measurement of the whole bone by defining a ROI that only contains the bone marrow. Analogously, the value of pure bone is derived from the images. The magnification for these measurements is given in table 2.3. Given that a whole CT scan at one energy takes about 2 h during which the biological sample is not cooled, the number of applied acceleration voltages is limited to two in order to keep the sample in a comparable state for all measurements. Firstly, a setting of 50 kV peak acceleration voltage and 32 mA is chosen, secondly the X-ray tube is set to 70 kV and 7 mA. The fat was frozen for two days and then defrosted before the calibration measurements. Like in the previous section, the images are cut using a circle mask in order to remove the plastic tube. The resulting calibration values for the four tissue types are plotted in figure 3.8. The shaded areas indicate the standard deviation of the data, the standard error is negligible. In the attenuation image, the mean values of the four materials differ noticeably, while fat and muscle values are most similar. However, the standard deviation bands for muscle and fat overlap, making differentiation of single pixels difficult. Bone has a much higher refractive index decrement than the other softer materials, as can be seen in figure 3.8b. Again, the mean values of the matierals have differentiable values, but the standard deviation bands overlap for fat and muscle, and additionally for bone marrow. The analysis of the dark-field signals allows no differentiation at all between the mean values of fat and muscle and none at the low energy between bone and bone marrow. Additionally, the error band of the dark-field signal is relatively large in comparison to phase and attenuation. The outlines of the standard deviation intervals that are shown visualise that it is impossible to allocate one pixel to one material unambiguously. Therefore, again the attenuation and phase image were utilised in the allocation algorithm as they have less overlapping values.

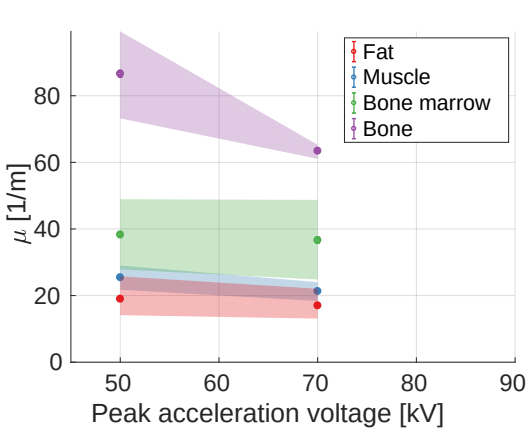

(a) Attenuation coefficient μ.

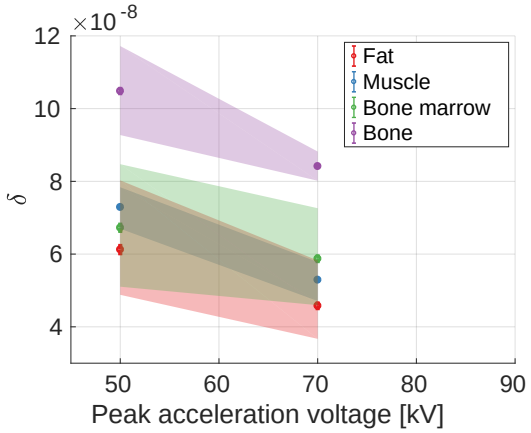

(b) Refractive index decrement δ.

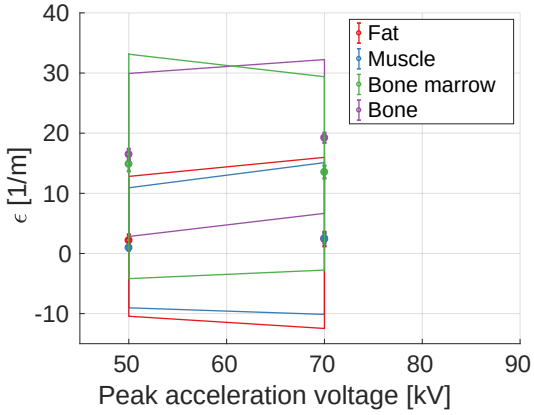

(c) Dark-field coefficient ϵ.

Figure 3.8: Calibration measurements for the porcine rib at two different peak acceleration voltages. The plotted material values are mean values of the separate measurements of fat, muscle and bone with bone marrow. The shaded areas indicate the standard deviation of the values. For the dark-field coefficient in **(c)**, only the outlines of the areas are shown for clarity. The standard error is of an order of one hundredth of the values and therefore negligible.

Finally, an intact rib is also measured inside a plastic tube and the material allocation algorithm is applied to the data. With this object, in contrast to the separate muscle, fat and bone measurements, the tube is distorted by the rib making it non-circular and hard to cut precisely from the image. Thus, the circle mask has to remove a small part of the object as well in order to ensure that there is no plastic in the image. A slice of the resulting CT image of the whole rib taken at at the high energy is shown in figure 3.9. The unmodified attenuation and phase images are contrasted with the images where the ring artifacts have been removed with the algorithm described in section 2.2.2.2. It can be seen in figure 3.9c and figure 3.9d that the ring artifact removal algorithm successfully removes the concentric rings. However, it also increases the object size radially and evens out details in the bone marrow, where thin bone structures can be seen in the non-modified image, as is shown in figure 3.9a and figure 3.9b. Therefore, for the allocation algorithm at first the non-corrected images are used.

In figure 3.11a, the result of the allocation algorithm can be seen. Four materials were differentiated using the non-corrected images at both photon energies. It can be noticed that the allocation of bone pixels works well, but there are almost no bone marrow pixels visible inside the bone. On the other hand, pixels outside the bone are allocated to be bone marrow, which cannot represent the actual situation. Furthermore, muscle, fat and bone marrow are mixed in a way that is not anatomically explicable. Therefore, it can be concluded that the separation of soft tissues remains challenging in DEPC-CT as well. The resulting volume proportions from the allocation of the whole object, i. e. 437 CT slices, are listed in table 3.3. There are no values to compare these results to, but one can assess the values by looking at the CT images. The bone percentage seems reasonable, as well as fat, that is barely present in the CT images of the object. The most striking result is that, although in the attenuation and in the phase image, there clearly is bone marrow present, the bone marrow percentage is lower than that of muscle over the whole object. Thus, bone marrow is probably underestimated, while on the other hand, too many pixels are allocated as muscle. This could be due to ring artifacts, as the allocated image clearly features concentric rings along which the same material is identified, regardless of the anatomical structure.

In order to test this hypothesis, the images were corrected for ring artifacts and the allocation was applied to these images. The calibration data was also corrected for ring artifacts to assure consistent values used for the allocation (see figure 3.10). In the phase shift data, the errorbars are much larger than in the respective calibration done for non-modified images. Because of the large standard error, only bone can be differentiated by looking only at the phase shift properties, while all other materials' values overlap. However, the resulting allocated image that is shown in figure 3.11b gives comparable results that are not less unambiguous than without the correction. The same holds for the quantitative analysis of the two data sets that is contrasted in table 3.3. The erroneously allocated fat and muscle pixels inside the bone are still present in the corrected image as well. The same is true for the bone marrow pixels outside the bone that can be observed in the ring artifact corrected image, too. Furthermore, there are no major discrepancies between corrected and raw images. Therefore, correcting the ring artifacts does not increase the accuracy of allocation in this case.

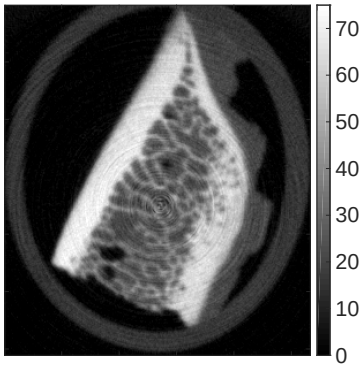

(a) Attenuation image, μ in m^{-1}, raw image.

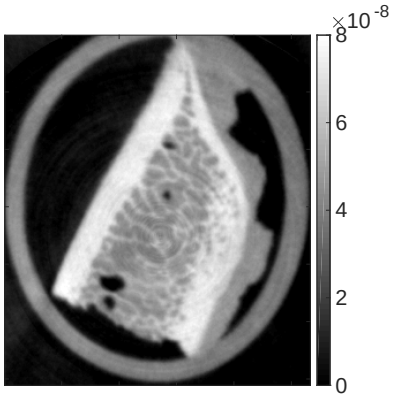

(b) Phase image, refractive index decrement δ, raw image.

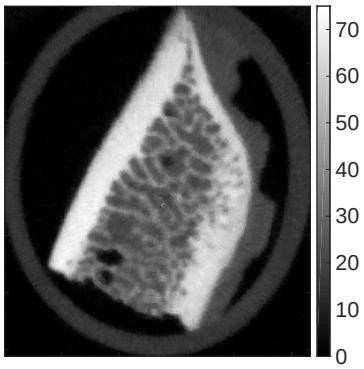

(c) Attenuation image, μ in m^{-1}, image corrected for ring artifacts.

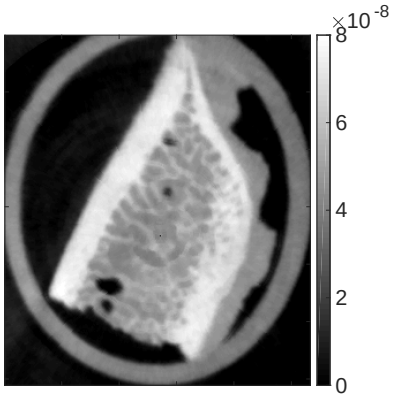

(d) Phase image, refractive index decrement δ, image corrected for ring artifacts.

Figure 3.9: One slice from the CT images of the whole rib obtained at 70 kV and 7 mA. The the bottom row, the images corrected for ring artifacts are shown with the same colour bar as the unmodified images. The ring artifact removal algorithm does lower the artifacts but also increases the object size and blurs details in the bone marrow.

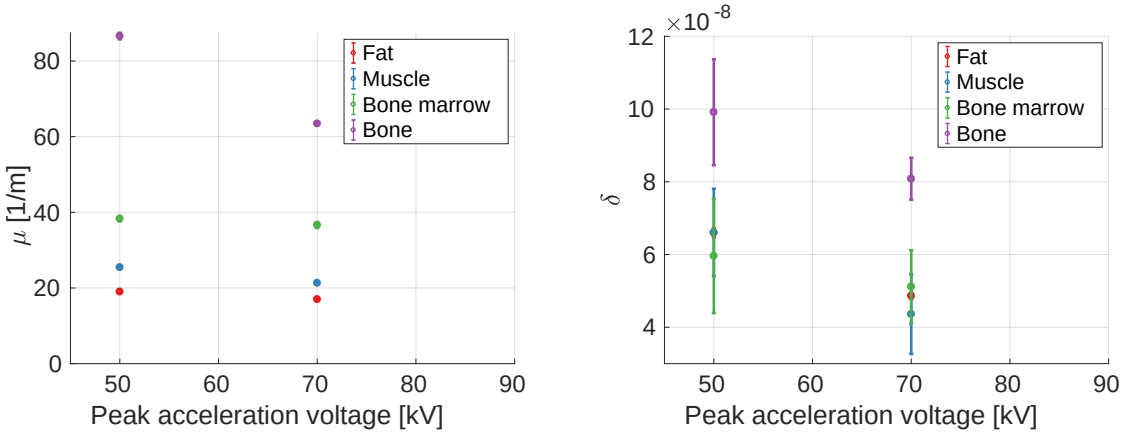

(a) Attenuation coefficient μ.

(b) Refractive index decrement δ.

Figure 3.10: Calibration measurements from figure 3.8 corrected for ring artifacts. The smearing of the algorithm increases the standard errors on the refractive index decrements significantly, whereas the standard error remains in the same order of magnitude for the attenuation values.

(a) Raw data.

(b) Data corrected for ring artifacts.

Figure 3.11: Result of the allocation algorithm applied to the rib CT data at 50 keV and 70 keV. In (a) the non-modified CT images were used with calibration data from figure 3.8, in (b) the CT images were corrected for ring artifacts using the algorithm from section 2.2.2.2 and allocated with calibration data from figure 3.10. The four materials are colour-coded as follows: red = fat, green = bone marrow, blue = muscle, purple = bone.

Table 3.3: Volume proportions resulting from the allocation algorithm applied to the rib CT measurements with and without ring artifact correction.

Material	Allocated volume proportion	
	Raw data	Ring artifact corrected data
Bone	78.4 %	77.6 %
Muscle	13.1 %	12.5 %
Bone marrow	5.2 %	4.3 %
Fat	3.6 %	5.6 %

3.2 Renal calculi

3.2.1 Clinical relevance

Urolithiasis Kidney stone disease is an illness that increases globally due to changes in dietary practices as a reflection of the standard of living [13]. In Germany, prevalence (number of cases alive) was 4.7 % of the adult population in 2000 [45]. When a patient has urolithiasis, crystalline sediments are formed in the renal pelvis. Renal calculi (kidney stones) can comprise different materials, the most common ones are Calcium oxalate and Uric acid. The ocurrence rate for different mineral compositions are listed in table 3.4. There can be pure and mixed stones, that are composed of several materials.

Table 3.4: The most common minerals in renal calculi and their occurrence rates [45, 46].

Chemical name	Mineral name	Chemical formula	Percentage
Calcium oxalate monohydrate	Whewellite	$CaC_2O_4 \cdot H_2O$	70-75 %
Calcium oxalate dihydrate	Weddellite	$CaC_2O_4 \cdot 2H_2O$	
Uric acid	Uricite	$C_5H_4N_4O_3$	10-15 %
Magnesium ammonium phosphate	Struvite	$MgNH_4PO_4 \cdot 6H_2O$	10 %
Calcium hydroxyl phosphate	Carbonate apatite	$Ca_5(PO_3)_3(OH)$	7 %
Calcium hydrogen phosphate	Brushite	$PO_4 \cdot 2H_2O$	1 %

Localisation and Treatment In clinical practice, renal stones are localised before surgery using CT or Dual Energy CT (DECT). During surgery, conventional X-ray radiography is used to supervise the successful removal or fragmentation of the calculi. During certain other treatments, ultrasound is used to find the stones. There are two main methods to remove the stones surgically. The most used is ureterorenoscopy (URS), where the stone is fetched through the urinary tract using an endoscope. If the stone is too big, percutaneous nephropitolapaxy

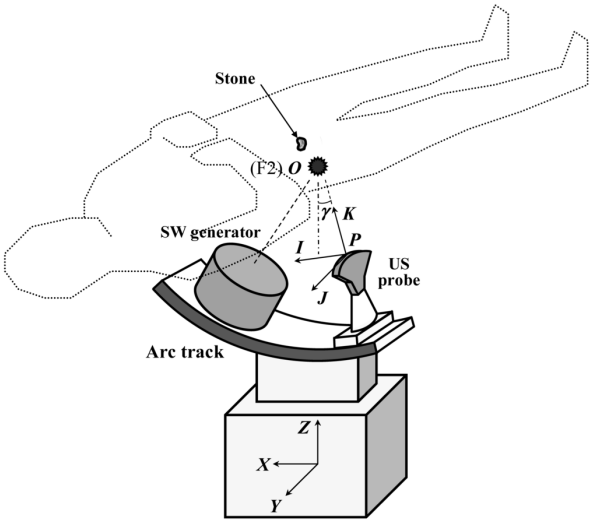

Figure 3.12: Schematic representation of the ESWL technique. The supersonic shockwave (SW) is generated outside of the body and focussed onto the stone using ultrasound for localisation. Figure taken from [48].

(PCNL) can be performed, where the skin is punctuated close to the kidney. The calculus is then removed using an endoscope through the skin. Before using these surgical methods, however, there is another method called Extracorporal Shockwave Lithotripsy (ESWL). It is employed to fragment the calculi using shock waves that are generated outside of the body. ESWL was used in $\geq 50\,\%$ of all stone treatments worldwide in 2011 [47]. A schematic depiction of the process is shown in figure 3.12. Localisation of the calculus is done via ultrasound, another widely used method is fluoroscopy [47]. After successful fragmentation into smaller pieces, stones are more likely to pass without surgery. Different stone minerals respond differently to ESWL treatment. Generally, the treatment works better on smaller and softer stones. For Whewellite, Cystine and Brushite stones, there is a very small chance of successful fragmentation by ESWL [47]. Another non-invasive treatment is oral chemolitholysis that can dissolve Uric acid stones by alkanisation of urine [47].

Challenges for radiology As mentioned above, X-ray radiography is used during surgery to locate kidney stones. Most materials are radiopaque, like Whewellite, Weddellite and Brushite, or at least have poor radiopacity (Apatite). Uric acid, however, is radiolucent, having similar attenuation properties to water and soft tissue, which means it cannot be detected in X-ray radiography [45]. In CT, Uric acid stones are visible, although they have a very low contrast to the surroundings. Combining ocurrence data from table 3.4 with that information, only about $60\,\%$ of renal stones are visible in regular radiography [49]. A technique is needed by which radiolucent stones can be detected during surgery.
Another challenge for imaging is the fact that ESWL efficiency and the success of other treatment methods depend on the stone composition. In order to decide on the most promising method,

it is helpful to know the minerals the stone comprises. Partially, this is already done with Dual Energy CT scans that can identify Uric acid stones in vivo [50]. As already discussed in section 2.2.1, Dual Energy methods work particularly well when the involved materials have very different attenuation properties at high and low photon energies. This is the case for differentiation of Uric acid from non-Uric acid stones, as the former consist only of light chemical elements (H, C, N, O, compare table 3.4), whereas the latter include heavy elements (P, Ca, S) [16]. Many studies have shown that Uric acid can be differentiated from other materials using Dual Energy CT scans: [50–53]. They also rely on the different HU of different materials at high and low energies. According to [50], differentiation of Uric acid/non-Uric acid is realised by a diagram whose axes scale the HU at each energy respectively. A gauge line that bisects the diagram through the HU data point of urine/water divides the two stone groups. They are differentiated based on their location relatively to the bisection line in the diagram. Furthermore, a Dual Energy Index (DEI) is calculated from the HU at both energies that is used to generally identify certain materials:

$$\mathrm{DEI} = \frac{x_{\mathrm{low}} - x_{\mathrm{high}}}{x_{\mathrm{low}} + x_{\mathrm{high}} + 2000} \ , \tag{3.4}$$

where x_{low}, x_{high} are the CT densities of the material in HU at the low and high tube acceleration voltage. The drawback of this method is that while Uric acid can be distinguished very well from the rest, mixed stones, Struvite, Cystine and calcified stones have a large overlap in their DEI [50]. Thus, the latter materials cannot be distinguished by conventional DECT.
As a first extension of the regular DECT methods, there was an approach by Scherer et al. using phase-contrast technology to differentiate Uric acid from calcium oxalate and mixed stones via the absorption-to-scattering ratio, which was carried out on extracted stones in a laboratory interferometer [17]. However, there is a need for precise determination of mineral compositions by radiological means that goes beyond the Uric acid/non-Uric acid differentiation before treatment to ensure the best possible method be applied.

3.2.2 Seperating ESWL resistant and non-resistant materials

As mentioned above, certain materials are more prone to breaking during ESWL therapy than others. Nine different renal calculi samples[1] were measured projectively and in DEPC-CT in order to examine the possibility of identifying the different types of stones. All patients involved were informed, and consented in writing to the participation in the study. The mineral composition of the samples was determined chemically via infra-red spectroscopy by MVZ Weiden GmbH. In table 3.5, a complete list of the samples that were measured and of their mineral compositions is given. Most of the samples contained mixed stones, where in one of the mixed samples (0547494) the stones consisting of the two minerals could be distinguished by colour, allowing measurements of pure Uric acid and pure Weddellite (see figure 3.13). Of one sample, no spectral analysis was available so that the mineral composition remains unknown.

In order to have an overview, all kidney stone samples were measured first in the projective set-up described in section 2.1.1 in different plastic containers filled with 17 mm water. The

[1] The renal calculi samples were kindly provided by Dr. Wencke Losensky from Universitätsklinikum Erlangen, Urologische Klinik

Table 3.5: List of all renal calculi samples that were measured in this thesis and of their mineral composition determined by infra-red spectroscopy.

Internal code	Mineral composition	Abbreviation
0547451	10 % Whewellite 90 % Uric acid	10Wh90Ua
0547494	10 % Weddellite 90 % Uric acid	100Wd 100Ua
0550824	10 % Weddellite 90 % Carbonate apatite	10Wd90Ca
0548715	10 % Weddellite 90 % Whewellite	10Wd90Wh
0549752	20 % Carbonate apatite 30 % Weddellite 50 % Whewellite	20Ca30Wd50Wh
0549477	100 % Brushite	100Br1
0546000	100 % Carbonate apatite	100Ca
0548378	100 % Brushite	100Br2
0546552	unknown	–

Table 3.6: Tube settings for projective kidney stone measurements.

Peak acceleration voltage [kV]	40	50	60	70	80
Current [mA]	50	40	33	28	25

measurements were carried out at different energies and currents that are listed in table 3.6. The resulting attenuation, differential phase and dark-field images for 40 keV and 50 mA are shown in figure 3.14. The images shown are averaged over 5 iterations.

Figure 3.13: Picture of two renal calculi samples in the plastic containers that were used for the projective measurements. In the sample on the right (0547494), there are two types of stones that can be distinguished by colour, the yellow stones consist of Uric acid and the dark stone is made of Weddellite. The sample on the left (0546552) was not analysed by infra-red spectroscopy. The container diametre is $\varnothing \approx 2.5\,\mathrm{cm}$.

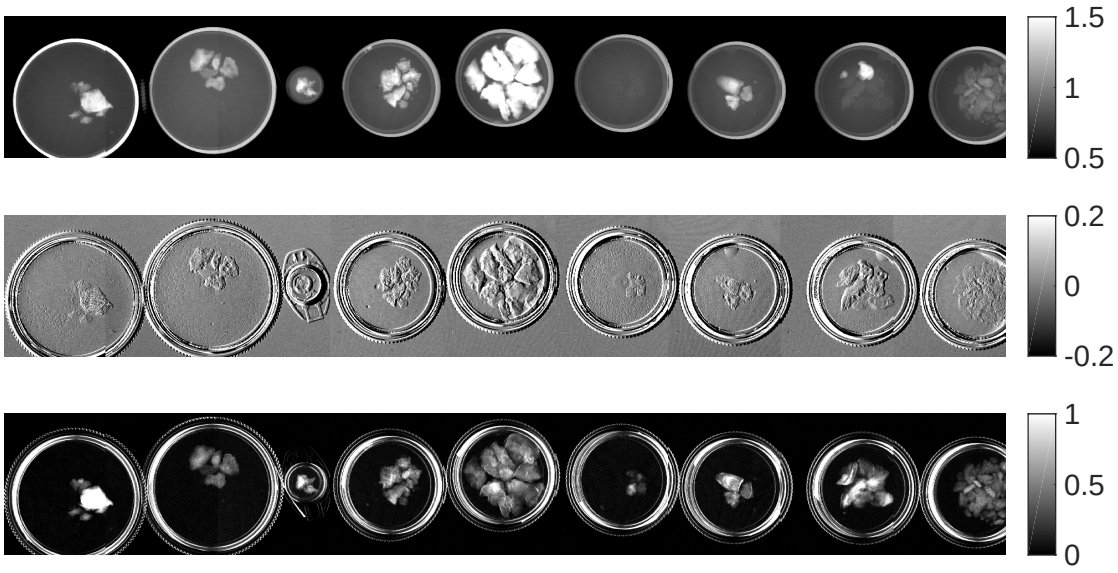

Figure 3.14: Projective images of all kidney stone samples listed in table 3.5, taken at 40 kV peak acceleration voltage and 50 mA. The top image shows the attenuation image, the middle one is the differential phase image, the bottom image shows the negative logarithm of the dark-field signal of the stones. The order of the samples from left to right is 10Wd90Ca, 10Wd90Wh, 100Br2, 100Br1, 10Wh90Ua, 100Ca, 0547494 (Uric acid and Weddellite), 0546552.

3.2.2.1 Radiographic dark-field measurements

In projective attenuation and dark-field images, the pixel values p_μ and p_ϵ represent the attenuation and dark-field coefficient integrated over the the object's thickness d. In case of a homogeneous object, this corresponds to a multiplication by the object's thickness:

$$p_\mu = \ln\left(\frac{I_0 \cdot \exp\left(\int_0^d -\mu \,\mathrm{d}x\right)}{I_0}\right) = \mu d \;, \tag{3.5}$$

$$p_\epsilon = \ln\left(\frac{I_0 \cdot \exp\left(\int_0^d -\epsilon \,\mathrm{d}x\right)}{I_0}\right) = \epsilon d \;. \tag{3.6}$$

As both images are obtained simultaneously, the pixels in the two images correspond to each other and can be compared directly. The kidney stones consist of a crystalline structure composed of one or more minerals and can be assumed to be homogeneous. Thus, by dividing the dark-field pixel values by those of the attenuation image, the quotient of ϵ/μ is obtained which is independent of the object's thickness at that particular position [17]. This method is applied to the projective image of the renal stones in water. The aim is to determine the quotients for all the stones and investigate whether they are material specific. This would allow the differentiation of minerals in radiography. The ROI in which the quotient is calculated is chosen manually for each sample. Two exemplary samples with ROIs are shown in figure 3.15.

The material values obtained in each pixel in the ROI in the attenuation and dark-field image are presented in figure 3.16. Out of the 10 different stone types (counting 0547494 twice for Uric acid and Weddellite), 4 pure samples were picked: Brushite (100Br1), Carbonate apatite (100Ca), Uric acid (100Ua) and Weddellite (100Wd). The ROI used on the Brushite stones

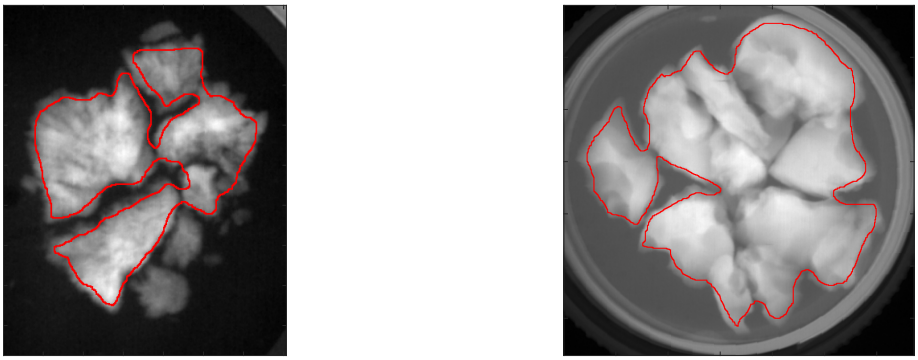

(a) Sample 100Br2 **(b)** Sample 100Br1

Figure 3.15: Attenuation images of two exemplary samples at 40 keV and 50 mA cropped from figure 3.14. The red lines indicate the ROIs that were used in order to calculate the ϵ/μ-quotient of the corresponding sample.

is also shown figure 3.15b. All other images were preprocessed similarly. The data for Uric acid, Weddellite and Brushite follows a linear distribution, for Carbonate apatite there is no clear trend. A linear fit of the data using Principle Component Analysis (PCA) yields the gradients of the linear functions, which are plotted for all tube settings in figure 3.17. The errors are calculated by error propagation of the variance of the principal component coefficients that is given by the eigenvalues of the corresponding covariance matrix of the data points. In table 3.7, the gradients of the linear fits are listed. The gradient of Uric acid differs most from the values of the other materials. It is also noticeable that for Uric acid, the gradient decreases towards higher energies, whereas it increases for all other materials. Carbonate apatite also has a significantly higher gradient than Brushite and Weddellite, which might be due to the fact that the underlying distribution of the data points in the scatter plot is non-linear at high attenuation values, which leads to a larger gradient. For Weddellite, the gradient relatively increases most over the energy range from 40 keV to 80 keV.

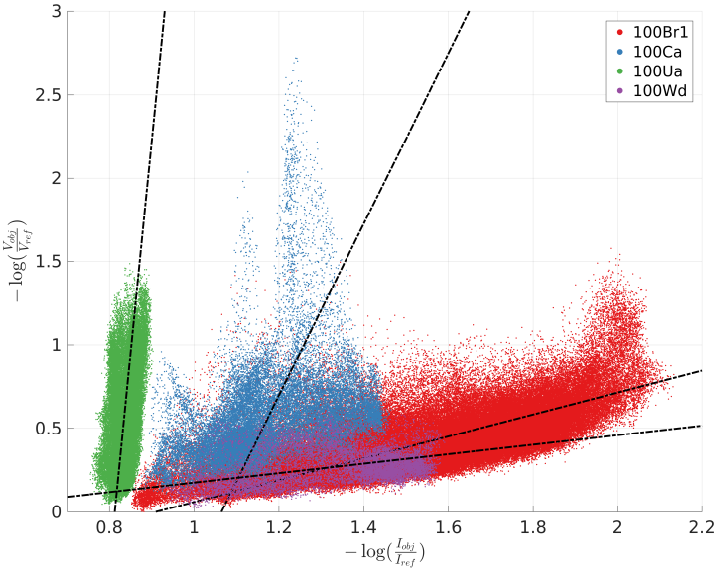

Figure 3.16: Scatter plot of 4 different kidney stone types comparing dark-field and attenuation values pixelwise. The images used were obtained projectively at 40 kV peak acceleration voltage and 50 mA. Fit values of the linear fits are given in table 3.7.

Checking for reproducibility of the dark-field/attenuation gradient, the data of the Brushite stone (100Br1) is compared to a second pure Brushite stone (100Br2) from a different patient (see purple lines in figure 3.18). The comparison shows, that the values are not consistent, leading to the conclusion that the gradient depends on other factors besides the mineral composition of the stone. Two stones from the same material could have different micro-structures and densities depending on the patient and the region where the stone was formed causing different dark-field and attenuation values.

The mixed stones are analysed in the same way as the pure stones with a PCA of the dark-field data over the attenuation values and the resulting gradients of the linear fits are shown in

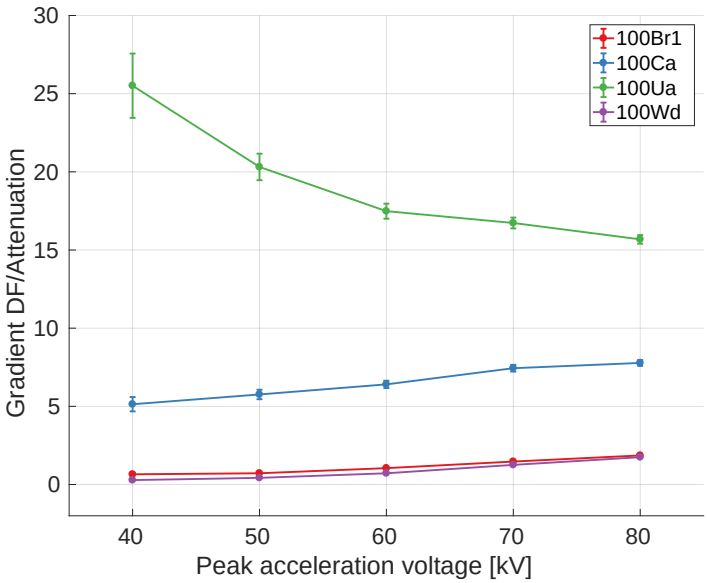

Figure 3.17: Line plot of the gradients of 4 different kidney stone types in the dark-field and attenuation value scatter plot from figure 3.16.

figure 3.18 for all acceleration voltages. The sample containing mainly Uric acid (10Wh90Ua) has the highest gradient, as expected from the measurements of the pure stones. Compared to the pure Uric acid stone, the gradient is enlarged by a factor of 2, which could be due to the 10% proportion of Whewellite. On the other hand, from the experience with the Brushite values that are not reproducible, this might be an effect caused by the the circumstance that the mixed sample originates from a different patient than the pure Uric acid stone. Comparing figure 3.17 and figure 3.18, it is observed that the gradient decreases for the mixed Uric acid stone (10Wh90Ua) over the energy range from 40 kVp to 80 kVp as it does for the pure Uric acid stone. All other mixed stones show increasing gradients for higher energies. This could be a way of identifying mixed calculi that contain Uric acid.

Comparing the results to those published by Scherer et al. [17], it can be confirmed that the dark-field pixel values over attenuation pixel values can be fitted by linear equations. However, no line through the origin can be fitted to the Uric acid data, in contradiction to observations by [17]. Furthermore, the measurements in this thesis confirm that the gradients m are very distinct for Uric acid and Weddellite. Evaluating the slopes quantitatively, the ϵ/μ-values obtained by Scherer et al. are $m_U = 7.69 \pm 0.59$ for Uric acid, $m_O = 1.03 \pm 0.47$ for Calcium oxalate and for mixed stones of unknown composition the slope is $m_M = 3.23 \pm 1.35$ measured at 40 kVp and 70 mA. These values are calculated from the μ/ϵ-values that are given in the literature. Although the slopes from the literature cannot be compared directly to the results obtained in this thesis due to different fit functions and due to different set-up parameters (gratings, distances, spectrum), they give an impression of the order of magnitude that would be expected. Another obstacle for comparison is the question whether the X-ray images of the renal stones in the publication were obtained in water or in air, which is not answered in the

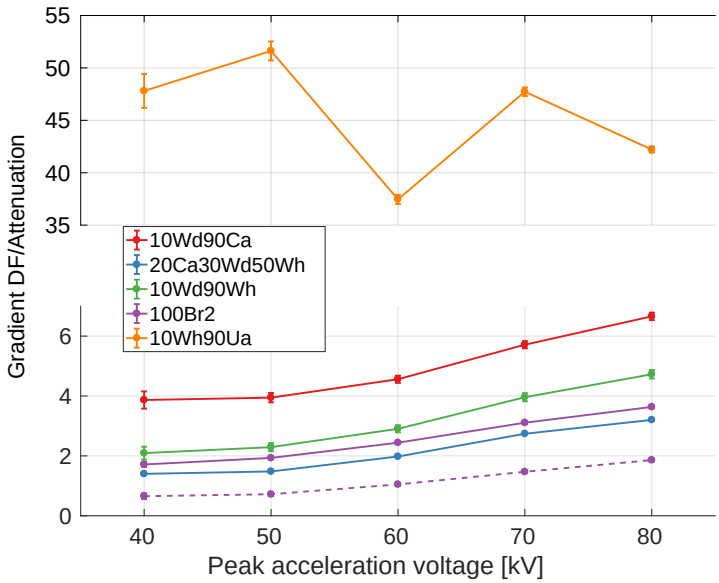

Figure 3.18: Line plot of the gradients of the mixed kidney stones and the second Brushite stone in the dark-field and attenuation value scatter plot. The dashed purple line indicates the value of the first Brushite stone (100Br1). Further explanation as to why the values for 10Wh90Ua are so much larger than the other samples' can be found in the text. In table 3.5, the mineral compositions of the samples are listed.

publication. Measuring the samples in water lowers the dark-field signal significantly compared to measuring in air. It is apparent that the fit results obtained in this thesis lie in a wider range of values than in the literature, therefore the absolute difference between the Calcium oxalate (Weddellite) and Uric acid values is even bigger. As it is not specified which minerals are included in the mixed literature samples, it is not meaningful to compare the "mixed stone" gradients from the literature directly to the ones obtained in this thesis. Nevertheless, even for mixed stones, coarse trends can be compared between these measurements and the literature. It is in agreement with the data obtained in this thesis, that the gradient of Weddellite is lower than that of any mixed stone. In conclusion, a linear correlation between dark-field and attenuation value, as well as gradients ranking Uric acid, mixed stones and Weddellite from highest to lowest, as were found in [17], can be confirmed by the measurements obtained in this thesis.

Table 3.7: Gradients m of linear fits to the data shown in figure 3.16.

Acceleration voltage	100Br1	100Br2	100Ca	100Ua	100Wd
40 kVp	0.65 ± 0.01	1.71 ± 0.08	5.13 ± 0.46	25.51 ± 2.06	0.28 ± 0.03
50 kVp	0.72 ± 0.06	1.93 ± 0.05	5.76 ± 0.31	20.31 ± 0.85	0.43 ± 0.02
60 kVp	1.05 ± 0.05	2.44 ± 0.05	6.41 ± 0.23	17.48 ± 0.48	0.72 ± 0.01
70 kVp	1.47 ± 0.04	3.11 ± 0.05	7.44 ± 0.21	16.73 ± 0.35	1.26 ± 0.01
80 kVp	1.86 ± 0.05	3.63 ± 0.05	7.78 ± 0.19	15.68 ± 0.28	1.75 ± 0.02

3.2.2.2 CT measurements

With the aim of differentiating more stones unambiguously than just Uric acid and non-Uric acid, the attenuation coefficient, the refractive index decrement, and the dark-field coefficient of the renal calculi are measured. From each kidney stone sample, one calculus is measured tomographically at three different tube settings in a glass vial filled with water using the CT set-up described in section 2.1.2. The energy settings for the CT measurements are listed in table 3.8, the magnification factor was $M = 1.8$ (see table 2.3). One resulting attenuation CT slice is shown as an example in figure 3.19 with the corresponding attenuation, phase and dark-field image. The object's attenuation coefficient μ, as well as the refractive index decrement δ and the dark-field coefficient ϵ are extracted from the images using an edge detection algorithm.

Firstly, the glass vial is cut out of the image using a circular mask as described above. Then, the edge detection algorithm identifies the object's edges, connects them and fills in the outlines in order to create a binary mask. Applying the mask to the original CT slice leaves only the pixels containing the stone with their original values, all other values are set to zero. Finally, a threshold value of $\mu_t = 23.1\,\mathrm{m}^{-1}$ (attenuation value of water) is set to exclude areas of ring artifacts in the surrounding water from the final image. This procedure is applied to all CT slices containing the sample. Consequently, the non-zero pixels are used to extract the object's attenuation coefficient, refractive index decrement and dark-field coefficient. An example for a resulting ROI is shown in figure 3.19a for one CT slice of sample 20Ca30Wd50Wh.

The resulting pixel values in the ROIs are evaluated for each stone by fitting a Gaussian distribution and by determining the mean and standard deviation of the distribution. Mean values of the Gaussian distributions are shown in figure 3.20. As the number of pixels is in the order of 10^5 to 10^6, the standard error is negligible. The standard deviation of the data is indicated by the shaded areas. In the phase image (figure 3.20b), only the standard deviation areas of the Brushite stones are plotted to show that they do not overlap. The rest of the standard deviations are omitted for clarity, as they all overlap with that of the lower Brushite values. It is noticeable that, in the phase image, the refractive index decrements of Weddellite and Uric acid coincide at 60 kVp and 70 kVp. For the dark-field coefficents, only the standard

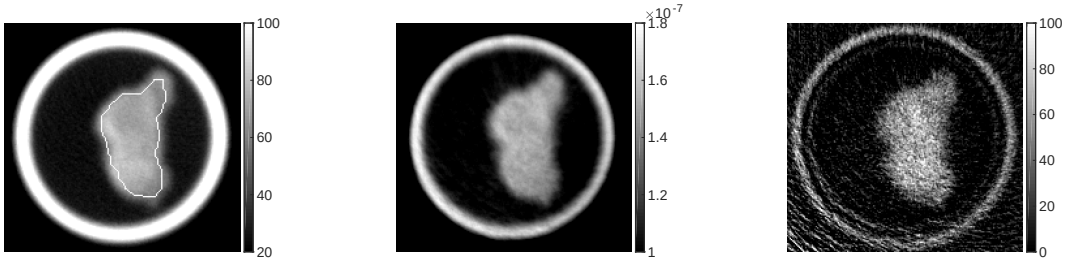

(a) Attenuation coefficient μ in m^{-1}.

(b) Refractive index decrement δ.

(c) Dark-field coefficient ϵ in m^{-1}.

Figure 3.19: CT images of the sample 20Ca30Wd50Wh. The white outline in (a) indicates the ROI that results from the edge-detection algorithm described in the text.

Table 3.8: Tube settings for CT kidney stone measurements.

Peak acceleration voltage [kV]	60	70	80
Current [mA]	20	8	4

deviation for Carbonate apatite is shown as an example. All other standard deviations lie in the same order of magnitude so that the areas overlap, thus they are omitted in the plot. It can be concluded from the calibration curves that differentiation of the materials based on the refractive index decrement and the dark-field coefficient may be difficult, considering that the values of the different materials do not differ significantly.

Dark-field based differentiation Analogously to the analysis of the radiographic data, the pixel values of the four pure samples are plotted with ϵ on the vertical axis and μ on the horizontal axis, as is shown in figure 3.21 for 60 kVp. The clear cut in the Uric acid data on the left side of the scatter plot is due to the threshold value. As mentioned above, pixels with $\mu < 23.1\,\mathrm{m}^{-1}$ are omitted from the analysis as they are undistinguishable from the surrounding water. Unlike in the radiographic data, no linear relationship between the two observables is expected, as the quantities μ and ϵ are already independent of the thickness of the sample. Therefore it is not necessary to form the quotient of the two quantities in order to obtain a thickness-independent quantity. The conspicuous topology of the Carbonate apatite sample is due to areas in the stone, where significantly higher dark-field coefficients were measured. These areas are located in the centre of the stone and they coincide with high attenuation coefficients.

The scatter plot is analysed for correlation by applying PCA in order to find the main axis of the data point distribution that is consequently used as semi-major axis of the ellipse that indicates confidence intervals. The ellipse's semiaxes denote the variance of the data, with

$$a = \sigma_x \sqrt{\chi^2(\mathrm{CI})}\ , \tag{3.7}$$

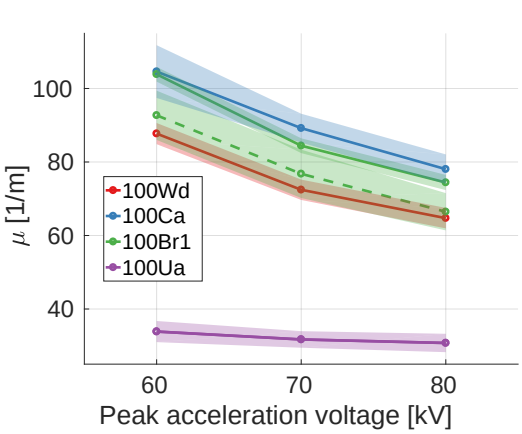

(a) Attenuation coefficient μ

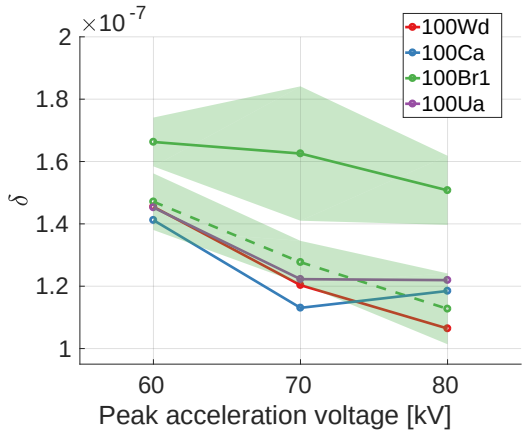

(b) Refractive index decrement δ

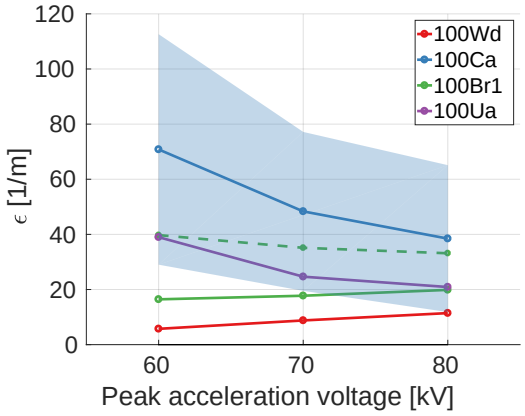

(c) Dark-field coefficient ϵ

Figure 3.20: CT values for 5 pure kidney stones measured at different peak acceleration voltages. The dashed line indicates the values of the second Brushite sample 100Br2. Shaded areas show the standard deviation of the data. In (b) and (c), only a few errorbands are shown for the sake of clarity. Corresponding currents can be found in table 3.8.

where a is the semi-major axis and σ_x stands for the variance of the data on the x-axis, assuming that the semi-major axis and the x-axis are parallel [54]. CI stands for the confidence interval within which the data points should lie. Using the cumulative χ^2-distribution for two degrees of freedom, the scaling factor of the ellipse is obtained. For a 95%-confidence interval the scaling factor is the square root of $\chi^2(0.95) = 5.99$, and for all points within one standard deviation it is the sqaure root of $\chi^2(0.683) = 2.30$ [55]. Equation (3.7) holds analogously for the minor semi-minor axis. From the angle by which the ellipse is tilted with respect to the x-axis, the correlation between μ and ϵ can be derived. An angle of $\beta = 0°$ indicates no correlation ($\rho = 0$), and $\beta = 45°$ stands for maximum correlation, therefore the correlation coefficient $\rho = 1$ [56]. Furthermore, the positions of the ellipses can be compared between the different stones.

In figure 3.22, the scatter plot of sample 100Ua is shown with the corresponding ellipses and distributions of the projections to the x- and y-axis. The main axis of the ellipse is tilted with respect to the x-axis by an angle of $\beta_{\mathrm{Ua}} = 71°$, which indicates a correlation between the two quantities. Furthermore, it can be seen that the observable ϵ follows a Gaussian distribution. Projected on the x-axis, the distribution underlying the attenuation values is not strictly Gaussian, as the distribution does not decrease strongly enough towards lower attenuation coefficients. This might be due to pixels at the edge of the object that have lower values and that were not excluded from the ROI by the edge finding algorithm. Nevertheless, a PCA of the data can be conducted and the resulting 95%- and 1σ-confidence intervals of all pure stones are shown in figure 3.23. The Weddellite data forms an angle of $\beta_{\mathrm{Wd}} = -9°$ with the x-axis, for Brushite (100Br1) that angle is $\beta_{\mathrm{Br}} = -11°$ and for Carbonate apatite it is $\beta_{\mathrm{Ca}} = 2°$. In comparison with the other minerals, Uric acid has the highest correlation between dark-field coefficient and attenuation coefficient. In the overview of the confidence intervals, the large overlap of the areas for Weddellite, Brushite (100Br1) and Carbonate apatite becomes apparent. This fact suggests that a scatter plot of dark-field coefficient over attenuation coefficient is not an unambiguous method to differentiate stone types. Therefore, scatter plots of the mixed stones are not investigated further. However, to check for reproducibility, the distributions of dark-field coefficients over attenuation coefficients for both Brushite stones are compared, which should be the same. It can be seen in figure 3.24 that the position and form of the confidence intervals do not agree completely for both Brushite stones from different patients. They come closer for higher energies but never completely overlap. Hence, what was already seen in the radiographic measurements is confirmed in CT: not only the mineral composition determines the stone's properties but they also depend on the patient. Probably, the properties differ due to different positions in the renal pelvis where the stone is formed or due to different growth speeds. Furthermore, the drawbacks of the confidence interval method become apparent in these plots, as the form of the ellipses does not accurately describe the data points. The data has a cut-off value at high attenuation coefficients that is not represented by the ellipses. Nevertheless, the confidence intervals indicate where the centre of mass of the data points lies.

From figure 3.22, it can be concluded that the dark-field and attenuation coefficients are distributed approximately normally. As a conclusion from the ellipses in figure 3.23, the positions of the pixel values in the scatter plot do not suffice to differentiate materials. Thus, going one step further, the quotient of the two coefficients ϵ/μ is examined in order to investigate whether it is characteristic of a material. The quotient of two normally distributed quantities

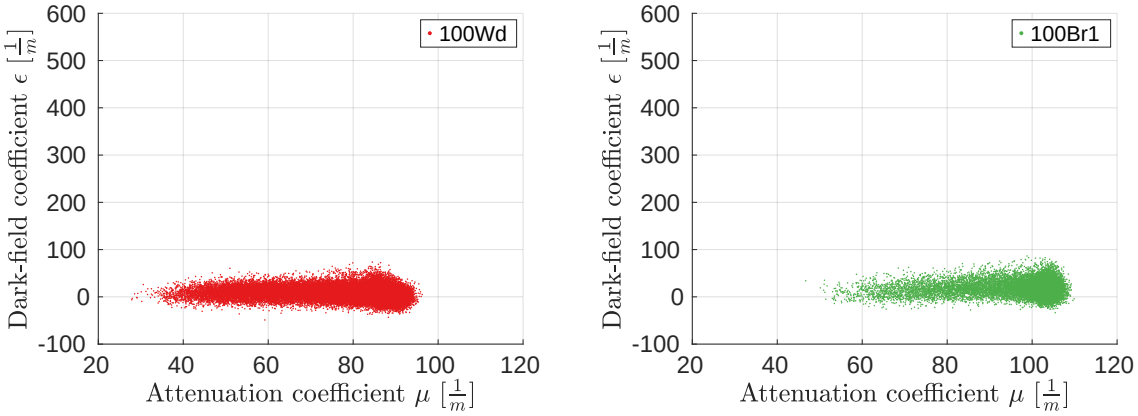

(a) Weddellite

(b) Brushite

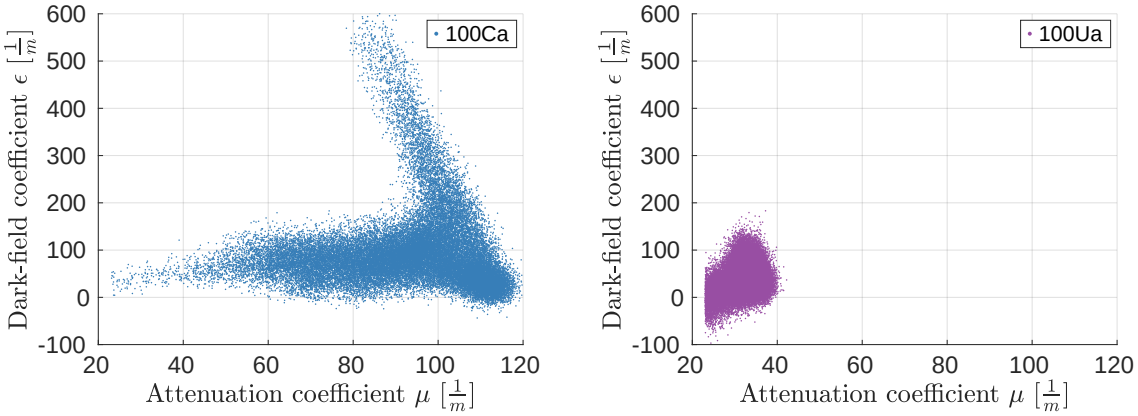

(c) Carbonate apatite

(d) Uric acid

Figure 3.21: Scatter plots of four different pure kidney stone types comparing dark-field and attenuation coefficients pixelwise. The data was obtained in CT at 60 kVp and 20 mA.

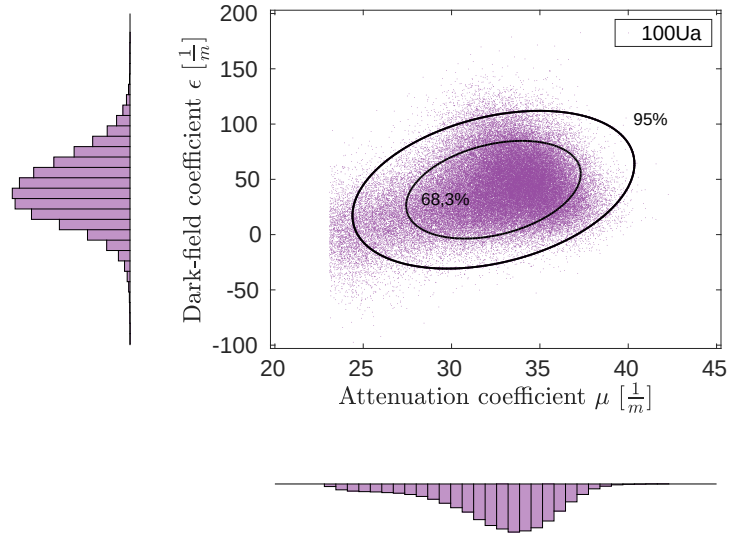

Figure 3.22: Scatter plot of the Uric acid stone comparing dark-field and attenuation values pixelwise. The outer ellipse indicates the area of the 95%-confidence interval, the inner one that of the 1σ-interval. The histograms are projections of the data points onto the x- and y-axis, respectively. The data has been obtained with a 60 kVp spectrum.

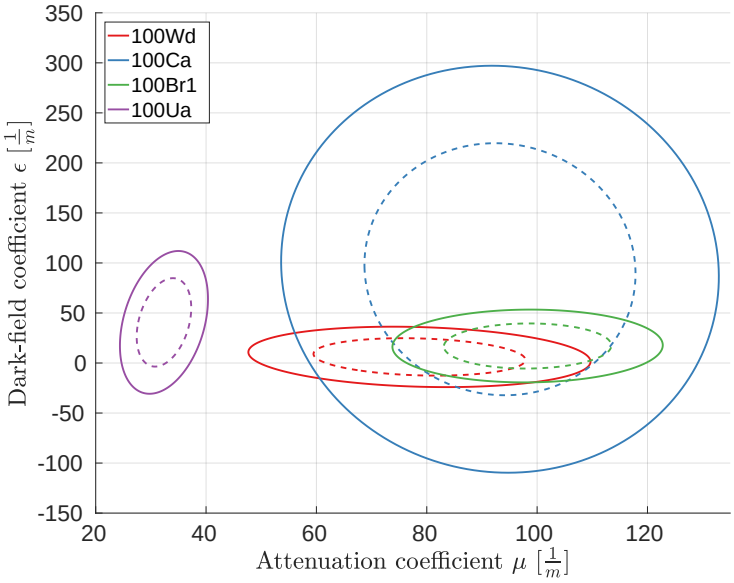

Figure 3.23: Confidence intervals of the scatter plots in figure 3.21 showing the dark-field coefficient over the attenuation coefficient for the pure stones. Solid lines indicate the 95%-confidence interval, dashed lines indicate the 1σ-interval.

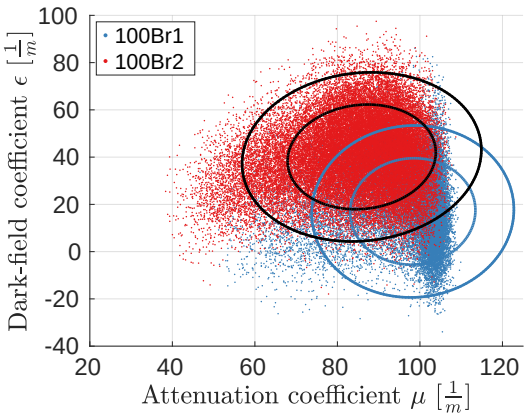

(a) 60 kV peak acceleration voltage

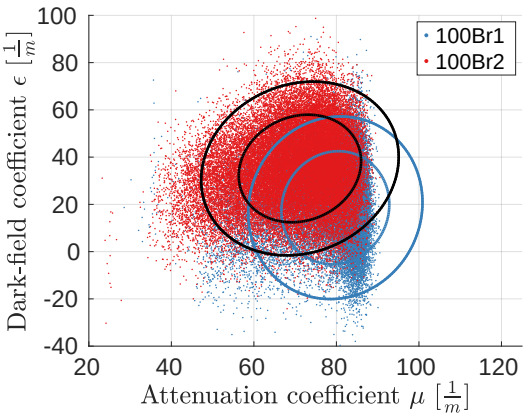

(b) 70 kV peak acceleration voltage

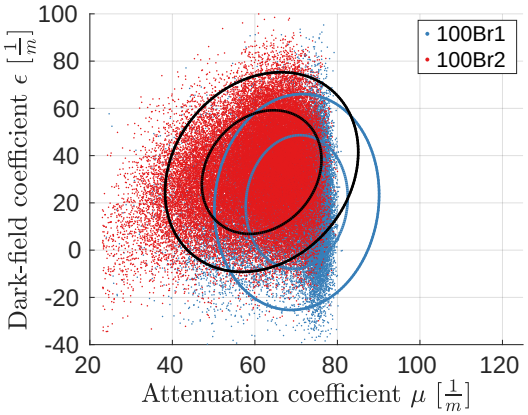

(c) 80 kV peak acceleration voltage

Figure 3.24: Scatter plots of dark-field vcoefficients over attenuation coefficients in CT for both Brushite samples from different patients. The data was obtained at three peak acceleration voltages. The outer ellipses indicate the 95%-confidence intervals, the inner ones indicate the 1σ-confidence intervals.

follows a Cauchy distribution, therefore it has no defined mean value or variance [56]. In this thesis, for the distribution of the quotients, the region around the peak is approximated by a Gaussian fit to the values, as the Cauchy distribution only differs from that approximation towards the edges. The resulting histogram of the quotients' abundance for the four pure stones at 60 kVp is shown in figure 3.25. The mean value and variance of the fit curves along with the number of pixels used for each stone are listed in table 3.9. From these values, expected quotients of the mixed stones can be calculated based on the knowledge of their composition:

$$\frac{\epsilon_\mathrm{m}}{\mu_\mathrm{m}} = \frac{\alpha\epsilon_1 + (1-\alpha)\epsilon_2}{\alpha\mu_1 + (1-\alpha)\mu_2} \ . \tag{3.8}$$

In this equation, $\alpha, 1-\alpha$ stand for the proportion of the material with dark-field coefficient ϵ_1, ϵ_2 and attenuation coefficient μ_1, μ_2, respectively. The quantities ϵ_m and μ_m represent the coefficients of the mixed stone. For a stone consisting of more than two known materials, the equation has to be adapted accordingly. As there is no stone that consists of pure Whewellite, the values of the mixed sample 10Wd90Wh alongside those of the pure Weddellite stone 100Wd are used to extrapolate the expected material values of Whewellite. These material values are in turn used for the calculation of expected values for stones comprising Whewellite, except for 10Wd90Wh. In figure 3.26, the histograms of the ϵ/μ-quotient of the mixed stones are shown at 60 kVp as an example. The quotients of the mixed stones and the expected values calculated from the equation (3.8) are shown in figure 3.27b. The expected values do not agree with the measured values for the mixed stones. As mentioned above, for the sample consisting of 90% Whewellite (10Wd90Wh), no expected value is calculated, because the material value for Whewellite was calculated from this stone. Analysing the quotients of dark-field and attenuation coefficient in dependence of the peak acceleration voltage, the values of different minerals come closer together for higher energies for pure stones (see figure 3.27a).

Examining the reproducibilty of dark-field/attenuation quotients for the same mineral from different patients, it is interesting to compare the two pure Brushite stones from different samples. Their histograms measured at 60 kVp are shown in figure 3.28, where it can be seen that the mean values differ significantly. The histograms barely overlap within their respective 1σ-intervals. For the other energies, the values do not coincide either, as can be seen comparing the green lines in figure 3.27a. Therefore, it can be concluded that the dark-field/attenuation quotient is not a suitable indicator of a material, as it also changes for different patients, like the absolute values of the coefficients. Reasons for that are probably again the different locations where the calculi are formed and the time they take to grow that both influence their micro-structure and therefore the dark-field coefficient. Furthermore, the quotient of a mixed stone apparently is not just the linear combination of the contributing minerals' quotients but differs, maybe due to a different crystalline structure of the mixed calculus.

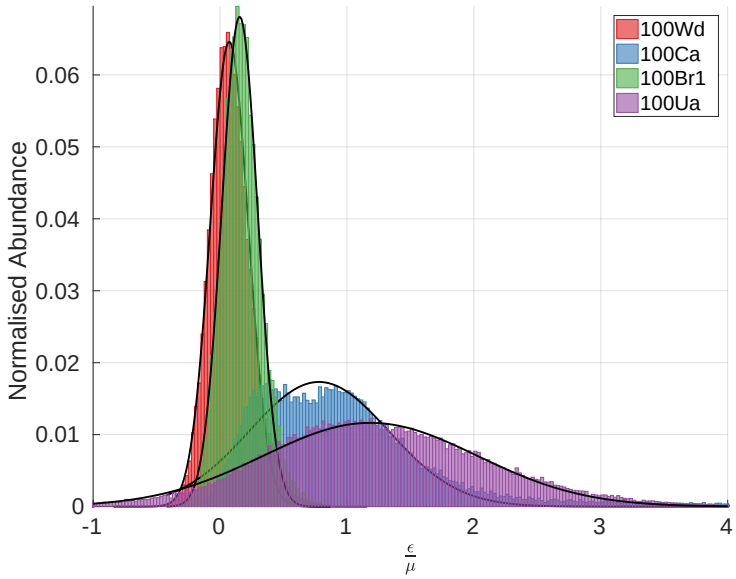

Figure 3.25: Distribution of the pixelwise calculated quotient of the dark-field coefficient divided by the attenuation coefficient for the pure stones. The values are extracted from the data obtained at 60 kVp. Histograms are fitted using a Gaussian distribution whose parameters are listed in table 3.9.

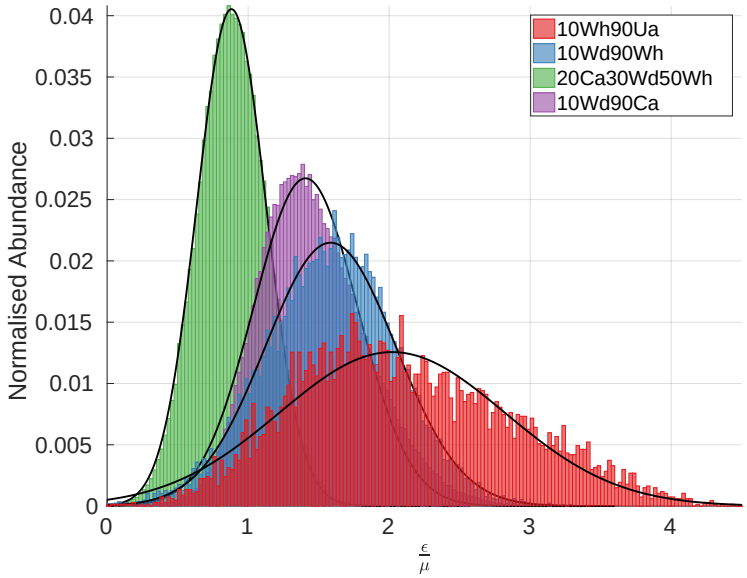

Figure 3.26: Distribution of the pixelwise calculated quotient of the dark-field coefficient divided by the attenuation coefficient for the mixed stones. The values are extracted from the data obtained at 60 kVp. Histograms are fitted with a Gaussian distribution.

Table 3.9: Fit parameters corresponding to the Gauss fits of ϵ/μ in figure 3.25 for the pure stones at 60 kVp.

Mineral	Mean value	Variance	Number of pixels
100Wd	0.06	0.15	62252
100Ca	0.77	0.55	43713
100Br1	0.14	0.14	30584
100Ua	1.16	0.85	122554

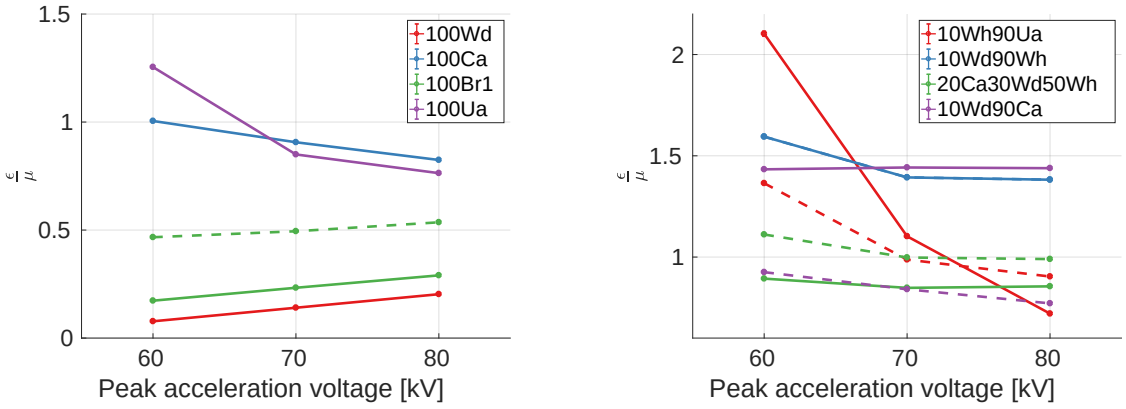

(a) Pure stones. The dashed green line shows the data of the second pure Brushite stone.

(b) Mixed stones. The dashed lines indicate the expected values calculated using equation (3.8).

Figure 3.27: Mean quotient of dark-field coefficient divided by attenuation coefficient for all stones measured in CT at different peak acceleration voltages. Standard errors lie in an order of magnitude of 10^{-3} and are therefore not discernible.

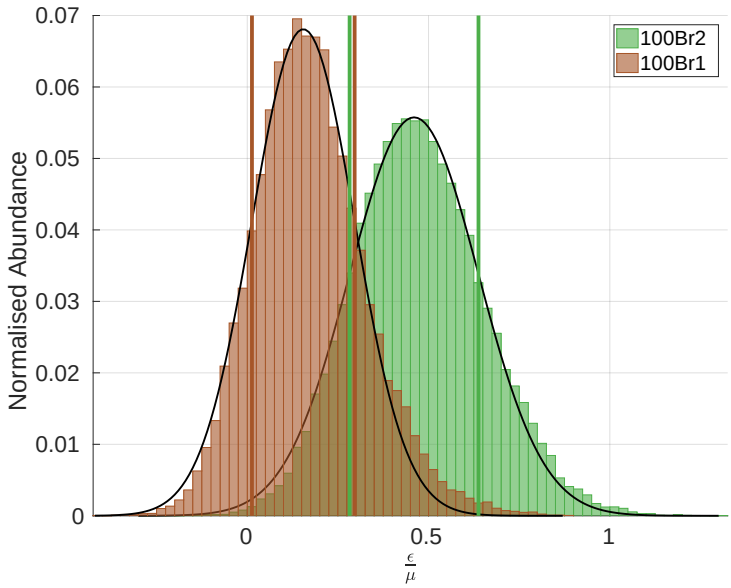

Figure 3.28: Distributions of the pixelwise calculated quotient of the dark-field coefficient divided by the attenuation coefficient comparing both Brushite stones from different patients. The values are extracted from the data obtained at 60 kVp. Histograms are fitted with a Gaussian distribution, the vertical lines indicate the 1σ-interval.

Refractive index decrement based differentiation After analysing the dark-field coefficients of the different renal calculi, analogous examinations are carried out for the refractive index property of the stones that is obtained in the CT measurements. The refractive index decrement δ of each pixel is plotted over the corresponding attenuation coefficient in figure 3.29. Again, the cut-off value at $\mu = 23.1\,\mathrm{m}^{-1}$ is due to a threshold that is set in the edge finding algorithm in order to exclude background (water) pixels from the ROI. In figure 3.30, the scatter plot is shown with projections of the data onto both axes for the Uric acid stone at 60 kVp as an example. As the histogram of the projections on the x-axis shows, the refractive index decrements' abundance does not decline symmetrically to both sides from the modus. Therefore, the data does not follow an underlying Gaussian distribution but the region around the value of highest abundance can be fitted with a Gauss fit. The attenuation values, on the other hand, are distributed approximately normally, as was already seen before. Considering the scale of the axes, the refractive index decrement and attenuation coefficients are not correlated, the main axis of the point cloud forms an angle $\beta \approx 0°$ with the x-axis.

The locations of the different stones' data are compared in figure 3.31 to see whether they lie in completely different regimes for different minerals. The other pure stones do not show correlation between the refractive index decrement and the attenuation coefficient either. Uric acid differs most from the rest of the materials due to its lower attenuation coefficient. All other stones' values lie in the same regime for the refractive index decrement and attenuation coefficient, which is why the affiliations cannot be distinguished. It is worth noting that in comparison to the dark-field scatter plots for CT, the range of phase shift values is much

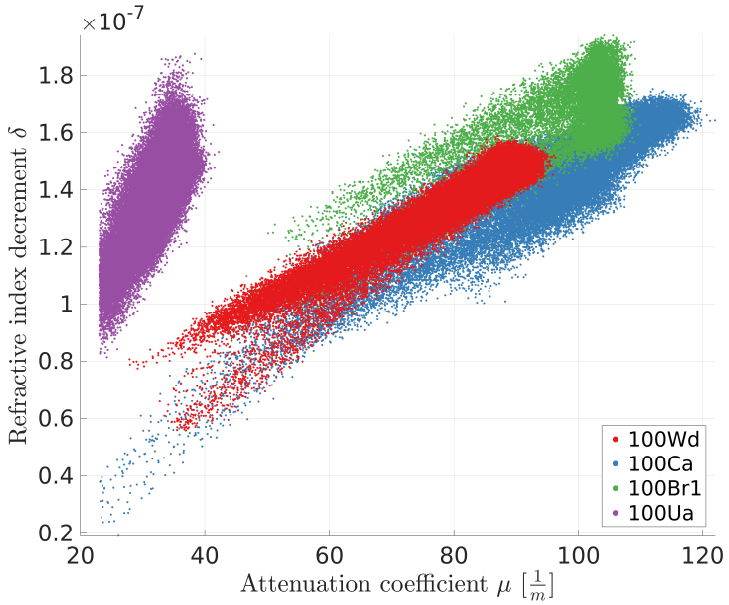

Figure 3.29: Scatter plot of four different pure kidney stone types comparing refractive index decrements and attenuation coefficients pixelwise. The data was obtained in CT at 60 kVp and 20 mA.

narrower than that of the dark-field coefficients (see figure 3.23). In figure 3.32, the positions of the confidence intervals of the refractive index decrement and the attenuation coefficient scatter plot of both Brushite stones (100Br1, 100Br2) are compared at different energies. For 60 kVp, the areas overlap greatly. Sample 100Br2 has more lower attenuation values, but apart from that, its data points lie almost completely within the confidence interval of the other sample. Going to higher energies, the separation of the ellipses increases.

Subsequently, the quotient of attenuation divided by refractive index decrement $q_p = \mu/\delta$ is examined. The histograms in figure 3.33 show the distribution of the pixelwise calculated quotients in the pure samples. Again, the distribution that results from the quotients is approximated around the maximum by a Gaussian distribution. Out of the three acceleration voltages, the pure stone's quotients in the q_p-distributions differ from each other most at 70 kVp. Considering the mixed stones in figure 3.34, it is noticeable that the q_p-values of sample 10Wd90Wh do not follow a Gaussian distribution with one peak, but rather two Gaussian distributions, that are fitted to the data. As an overall q_p-value for 10Wd90Wh, the mean of the two peaks is used. It might be gathered that the two peaks originate from the two materials in the stone (10 % Weddellit, 90 % Whewellite) but from their proportions it cannot be explained why the two q_p-values have the same abundance. If the two peaks originated from the different minerals, the peak at $q_p = 55 \cdot 10^{-7}\,\mathrm{m}^{-1}$ would probably correspond to Weddellite ($q_p = 58 \cdot 10^{-7}\,\mathrm{m}^{-1}$ at 70 kVp) as its value is closest to the Wedellite value. The peak on the right should therefore be 9 times lower in amplitude than the peak at $q_p = 47 \cdot 10^{-7}\,\mathrm{m}^{-1}$. As this is not the case, there has to be another explanation for the distribution that underlies the values.

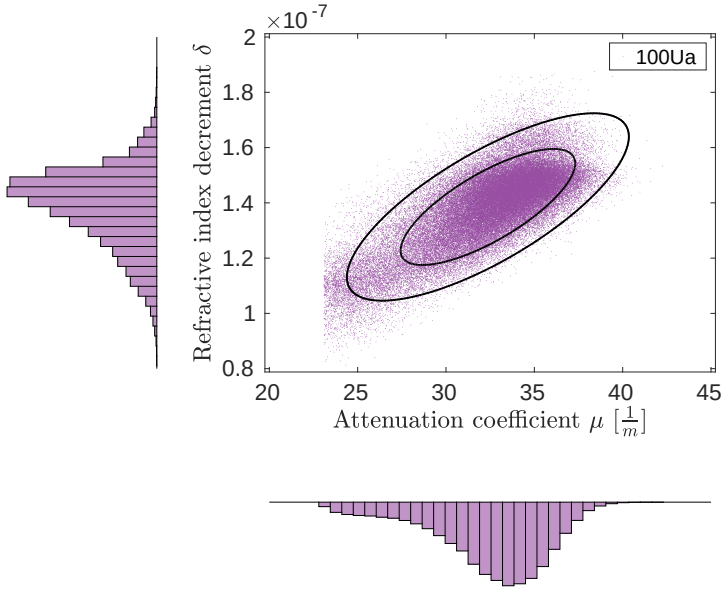

Figure 3.30: Scatter plot of the Uric acid stone comparing refractive index decrements and attenuation coefficients pixelwise for the data obtained at 60 kVp. The outer line indicates the area of the 95%-confidence interval, the inner line that of the 1σ-confidence interval. The histograms are projections of the data points onto the x- and y-axis, respectively.

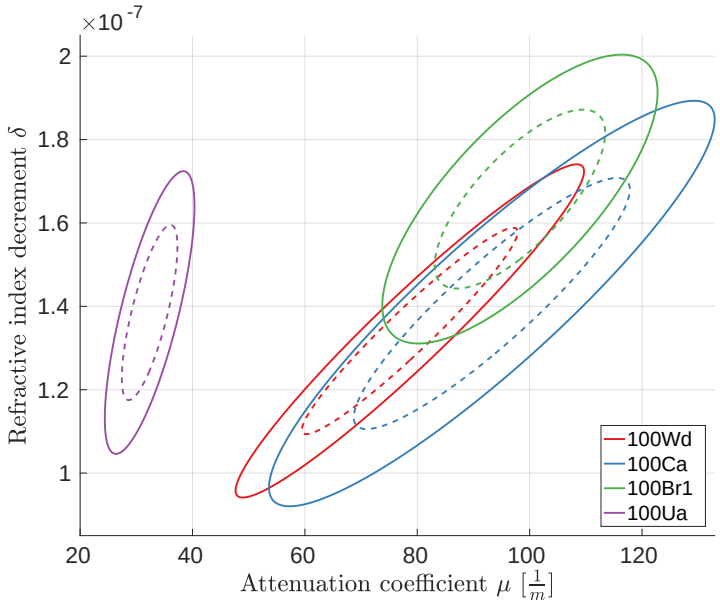

Figure 3.31: Confidence intervals of the refractive index decrement and attenuation data of the pure stones shown in figure 3.29. The solid lines indicate the 95%-confidence interval of the data points, the dashed line shows the 1σ-confidence interval. The CT data used for this evaluation was obtained at 60 kVp.

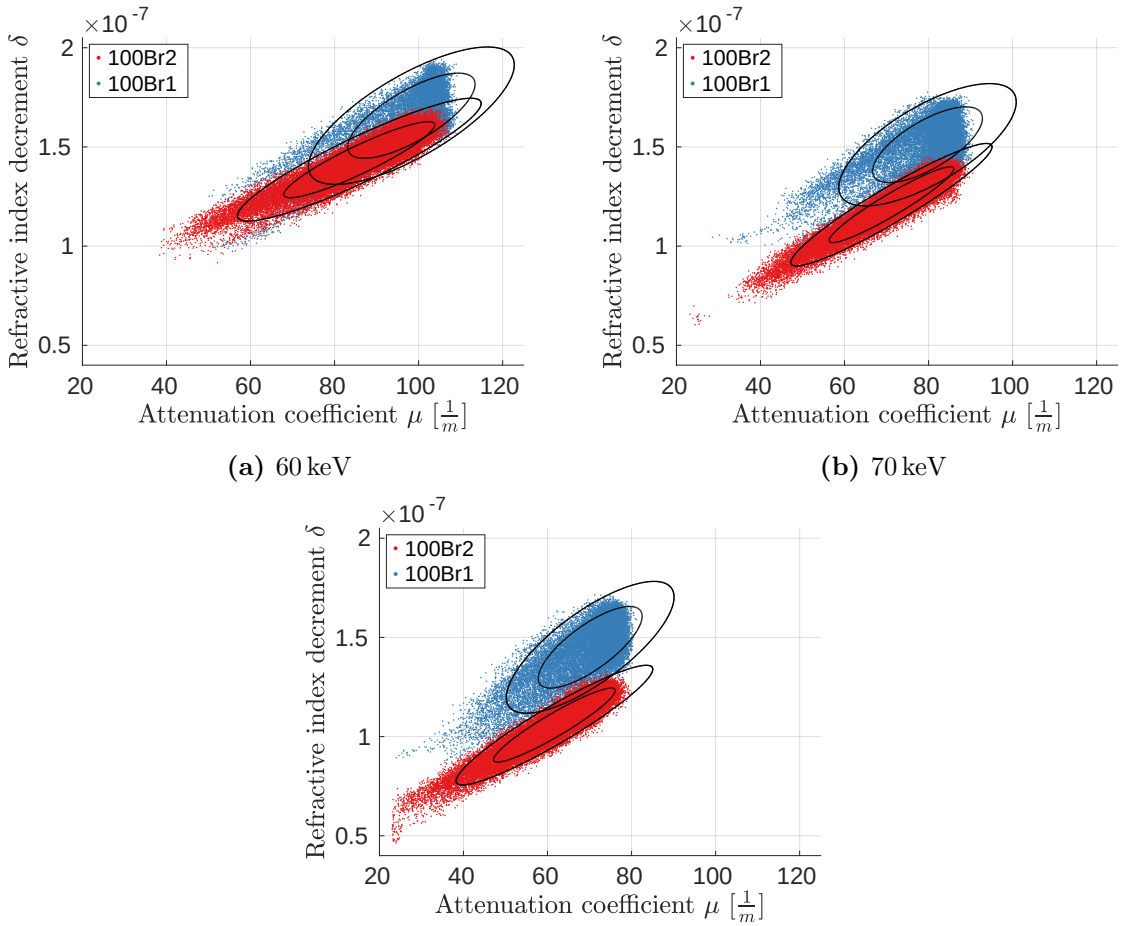

(a) 60 keV

(b) 70 keV

(c) 80 keV

Figure 3.32: Scatter plots of refractive index decrements compared to attenuation coefficients in each pixel for the two Brushite samples from different patients at three peak photon energies. The 1σ- and 95 %-confidence intervals are indicated by the lines.

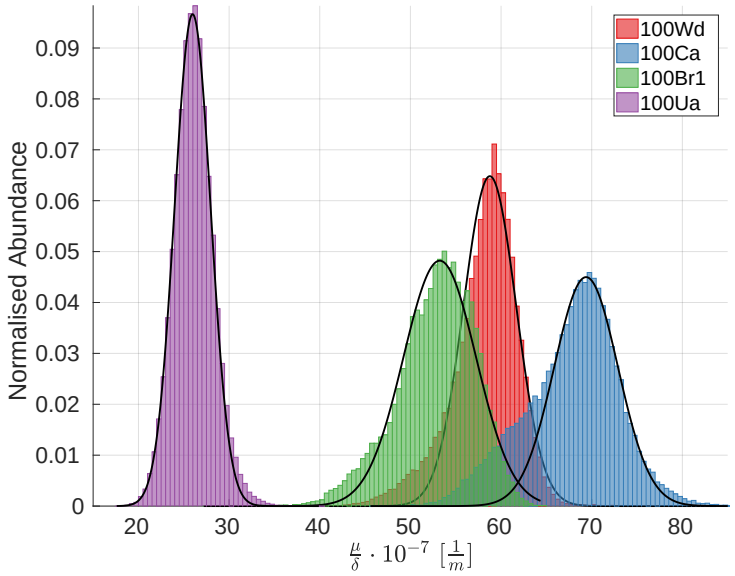

Figure 3.33: Distributions of the pure stones' pixelwise calculated quotients of the attenuation coefficient divided by the refractive index decrement. The values are extracted from the data obtained at 70 kVp, where the histograms of the materials differ most from each other. Histograms are fitted using a Gaussian distribution.

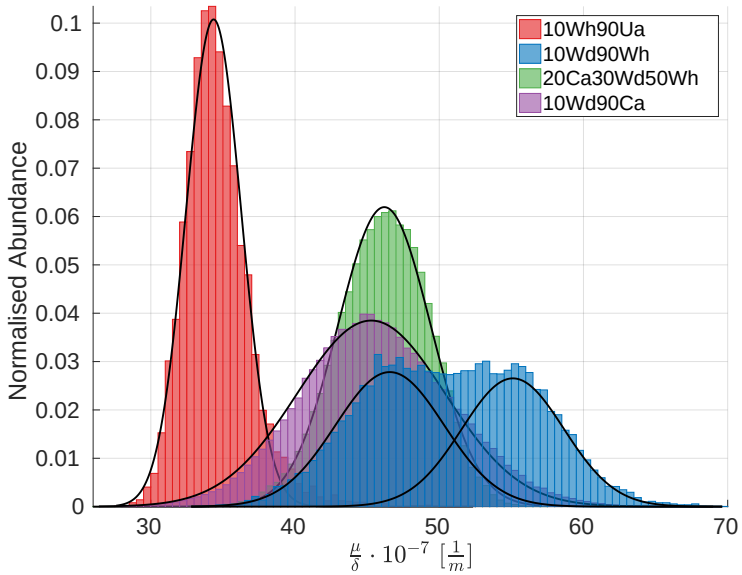

Figure 3.34: Distributions of the mixed stones' pixelwise calculated quotient of the attenuation coefficient divided by the refractive index decrement. The values are extracted from the data obtained at 70 kVp. Histograms are fitted with a Gaussian distribution. In the case of sample 10Wd90Wh, two Gauss fits are used to approximate the distribution of the data.

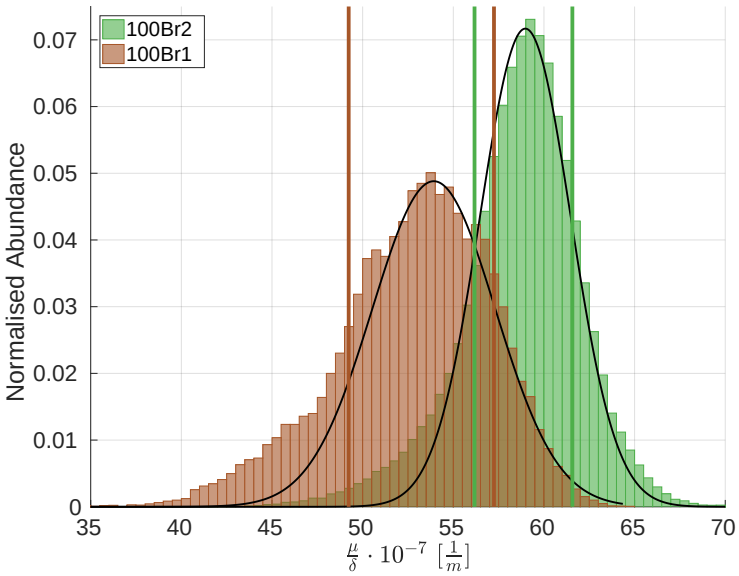

Figure 3.35: Distribution of the pixelwise calculated quotient of the attenuation coefficient divided by the refractive index decrement comparing both Brushite stones from different patients. The values are extracted from the CT data obtained at 70 kVp. Histograms are fitted with a Gaussian distribution in an interval around the peak, the vertical lines indicate the 1σ-interval.

For the Brushite samples, in agreement with the observations made for the confidence interval overlap (see figure 3.32), the mean values of the distributions are almost the same in both samples for 60 kVp and then deviate from each other more towards higher energies (see figure 3.36a). For comparability, the q_p-histograms of the Brushite stones are shown in figure 3.35 for 70 kVp, like the other stones' histograms. At the shown energy, the 1σ-intervals of the two distributions only overlap marginally. As the reproducibility of the q_p-value for the same mineral in different patients is higher than that of the dark-field coefficient over the attenuation, the phase image might be a better choice for material differentiation than the dark-field image.

Analysing the quotients' behaviour over different energies, no trend can be derived from the data of the pure stones (see figure 3.36a). What is most striking, is that the μ/δ-values of the Weddellite sample are almost the same as those of the second Brushite sample (100Br2). Therefore, the quotient cannot be used as a means to differentiating materials. Adapting equation (3.8) for the refractive index decrement/attenuation coefficient quotient, expected values are calculated for the mixed stones, that are indicated by the dashed lines in figure 3.36b. Again, for 10Wd90Wh from which the material value for Whewellite was calculated, no expected value is plotted. For the rest of the samples, there is no agreement between the expected and measured quotients q_p. The only prediction of the expected values that is confirmed by the measurements is that for sample 10Wh90Ua, the quotient q_p is lower than for all other mixed stones. The deviations of expected values of the samples containing Whewellite from

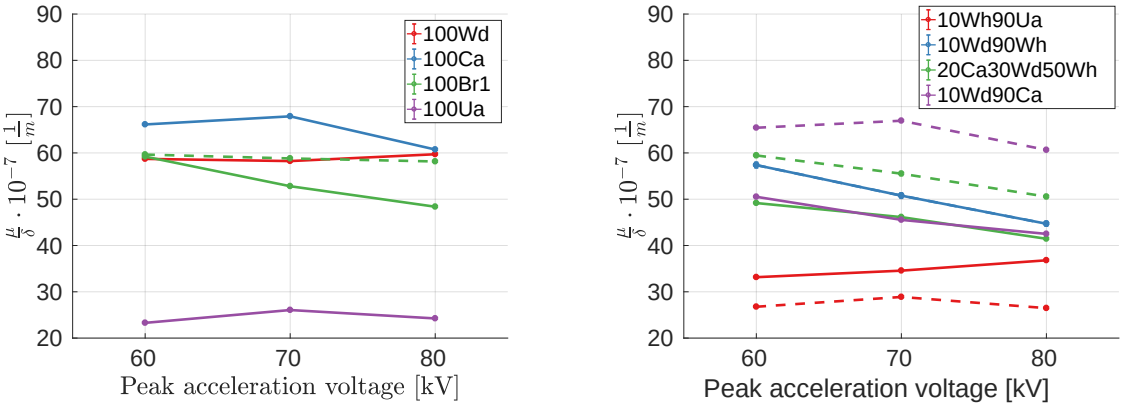

(a) Pure stones. The dashed green line shows the data of the second pure Brushite stone (100Br2).

(b) Mixed stones. The dashed lines indicate the expected values calculated using equation (3.8) adapted for q_p.

Figure 3.36: Mean quotients of the attenuation coefficient divided by the refractive index decrement for all stones measured in CT plotted over the different peak acceleration voltages. The standard errors lie in the order of one hundredth to one thousandth of the quotients, hence they are not discernible.

their measured values might be due to the fact that the material value for Whewellite is calculated from the 10Wd90Wh-values. This sample showed a non-Gaussian distribution, therefore its mean values might be erroneous. It is noticeable that the measured values for samples 20Ca30Wd50Wh and 10Wd90Ca coincide for all energies although they have different compositions. In addition to the almost identical quotient values of Weddellite and Brushite (100Br2), this result makes the quotient q_p useless for differentiation purposes of kidney stone mineral compositions, except for Uric acid.

Combining refractive index decrement and dark-field coefficient Not considering the attenuation coefficients of the stones, the dark-field coefficient and the refractive index decrement are put in relation in order to find differentiable properties of the stones. As was seen in the previous paragraphs, the attenuation coefficient mainly sets apart Uric acid from the other materials, because the mineral has a particularly low attenuation coefficient. In figure 3.37, the refractive index decrements of the four pure stones are plotted over their corresponding dark-field coefficients. As expected from the consideration of the attenuation properties of Uric acid, this mineral is not as easily distinguishable in this plot as in the ones comparing the attenuation coefficient to the refractive index decrement (see figure 3.29) and dark-field coefficient (see figure 3.21), respectively. However, this kind of visualisation opens a new possibility for the differentiation of Weddellite and Brushite. They are most distinguishable at 80 kVp, but the confidence intervals also only overlap marginally at the other energies (see overview in figure 3.38). Like in the previous section, the refractive index decrement is not correlated with the dark-field coefficient. From the plot, there seems to be an angle between

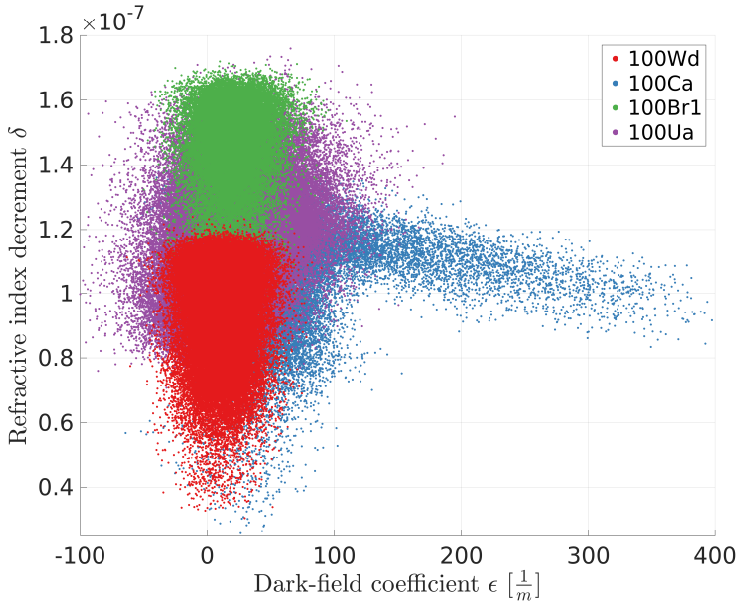

Figure 3.37: Scatter plots of four different pure kidney stone types comparing refractive index decrement and dark-field coefficient pixelwise. The data used was obtained in CT at 80 kVp and 4 mA.

the x-axis and the main axis of the Uric acid data, but considering the scales of the axes, the angle is still $\beta \approx 0°$.

By calculating the quotient of dark-field coefficient and refractive index decrement, a possibility to differentiate the materials is tested. In figure 3.39, the distributions of the pixelwise calculated quotients of the pure stones are shown. It is most noticeable that the quotients for Brushite (100Br1) and Weddellite are very similar, although these two materials were differentiable in the scatter plot. Apart from that, all other quotients also lie very closely together and the Gaussian fits to the distributions overlap. This fact does not change over the energies (see figure 3.40). Furthermore, the values for both Brushite samples from different patients do not coincide. Therefore, the quotient of the quantities dark-field coefficient and refractive index decrement is not a suitable measure for differentiation of kidney stone minerals. As a consequence, the distributions and line plots of the quotients for mixed stones are omitted here.

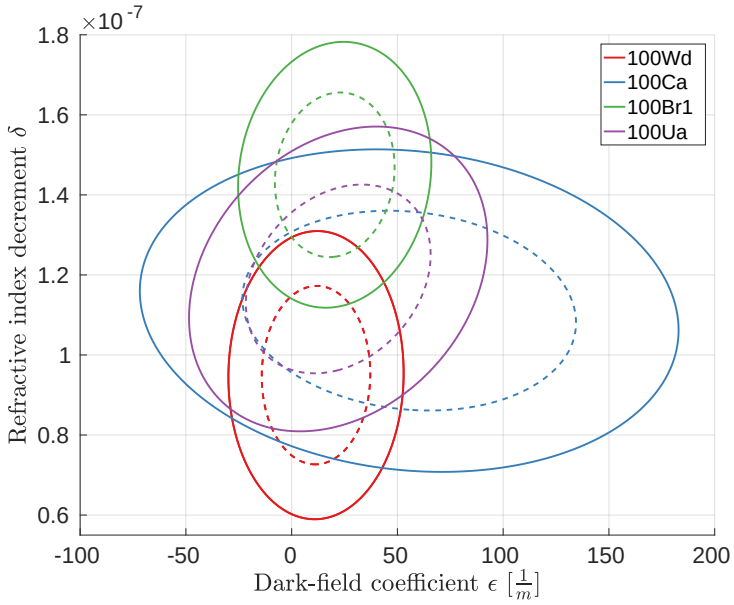

Figure 3.38: Overview of the confidence intervals of the pure kidney stone types from figure 3.37 comparing refractive index decrement and dark-field coefficient pixelwise. The data used was obtained in CT at 80 kVp and 4 mA.

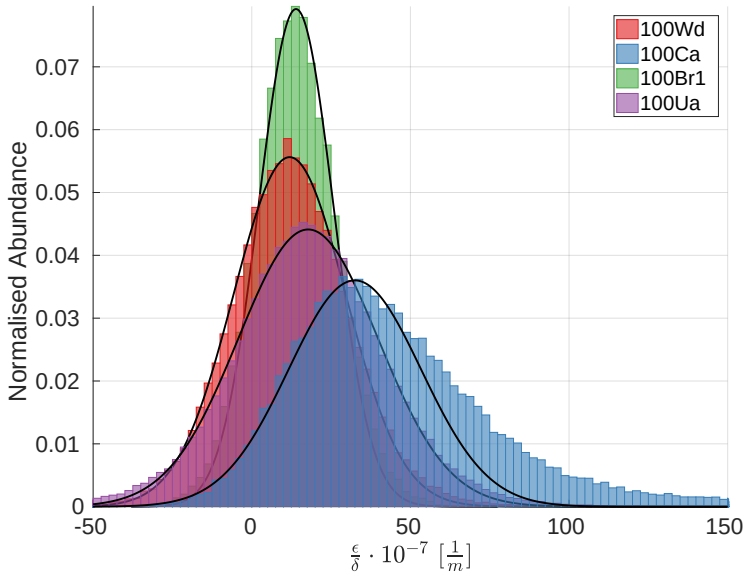

Figure 3.39: Distributions of the pure stones' pixelwise calculated quotients of the dark-field coefficient and the refractive index decrement. The values are extracted from the data obtained at 80 kVp, where the confidence intervals of Brushite (100Br1) and Weddellite (see figure 3.37) differ most from each other. The distributions are fitted using a Gaussian distribution.

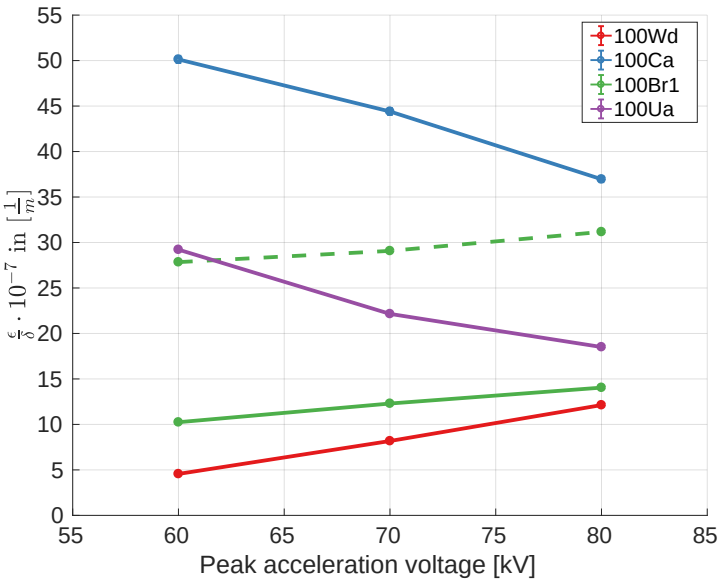

Figure 3.40: Mean of the Gauss fits in figure 3.39 of the quotients of the dark-field coefficient divided by the refractive index decrement for the pure stones measured in CT plotted over the different peak acceleration voltages. The dashed green line indicates the quotients of the second pure Brushite stone (100Br2). The standard errors lie in the order of one hundredth to one thousandth of the quotients, hence they are not discernible.

Conclusion on kidney stone differentiation via phase-contrast CT In the previous paragraphs, two methods of evaluation – scatter plots and quotients – with three combinations of quantities (ϵ/μ, μ/δ, ϵ/δ) were employed to investigate possibilities of differentiating kidney stone types based on their mineral composition. In all scatter plots considering the attenuation coefficient, Uric acid could be differentiated from the rest of the stones, providing the same advantages as regular Dual Energy CT. This is of particular interest for physicians, because Uric acid stones can be treated via oral chemolitholysis, which is a non-invasive treatment method. Using the refractive index decrement and the dark-field coefficient, Brushite and Weddellite can be sperated, which could be helpful in treatment planning, as Brushite is ESWL resistant, whereas Weddellite can be fragmented with this method. By forming quotients of the three CT properties of the stones, no additional information is gained. On the contrary, the quotients of different materials coincide, making it impossible to differentiate them. Furthermore, calculating expected values of mixed stones by taking into account the proportions of their pure constituents yields no agreement with the measured values. However, this is expected from the CT properties of the pure stones. For phase image and dark-field image in particular, the standard deviations to their values overlap, therefore it is expected that the quotients of these values do not bring better results. What makes the benefit of the phase-contrast CT measurement even more doubtful is the fact that the values and quotients for Brushite stones from two different patients differed significantly. Evaluating the approach to the samples, it should be confirmed in further measurements that stones from the same sample have comparable CT properties. In addition to that, the energy information of the measurement could be taken into account as a possible way of finding characteristic properties for certain minerals.

3.2.3 Increasing Uric acid visibility in CT

In conventional radiography, Uric acid kidney stones are not detectable. CT measurements are needed to localise this material, as its attenuation coefficient is very similar to urine, which surrounds the stone in the body. The sample 0547494 contains pure Uric acids stones, one of which is measured in CT as described in the previous section. From the attenuation and phase image, the contrast to noise ratio (CNR) is calculated. The CNR is a quantity that indicates how much an object stands out from the background. In this measurement, the background is water in the vial which is comparable to urine, the usual surrounding liquid of renal stones, in terms of attenuation coefficient and refractive index decrement. The attenuation and phase image of the Uric acid stone are shown for the same CT slice in figure 3.41. Using the ROIs of identical size that are indicated by the rectangles in the images, the CNR is calculated as follows

$$\mathrm{CNR} = \frac{|m_{\mathrm{obj}} - m_{\mathrm{bg}}|}{\sqrt{\sigma_{\mathrm{obj}}^2 + \sigma_{\mathrm{bg}}^2}} \,. \tag{3.9}$$

In this equation, m_{obj} stand for the mean value of the ROI in the object, m_{bg} for that of the background ROI. σ_{obj} and σ_{bg} are the corresponding standard deviations to the mean values. The CNR value is only comparable among images that were obtained under the same circumstances with only small differences between the images. Therefore, the absolute value is not meaningful and the CNR can only be used to compare several options relatively to

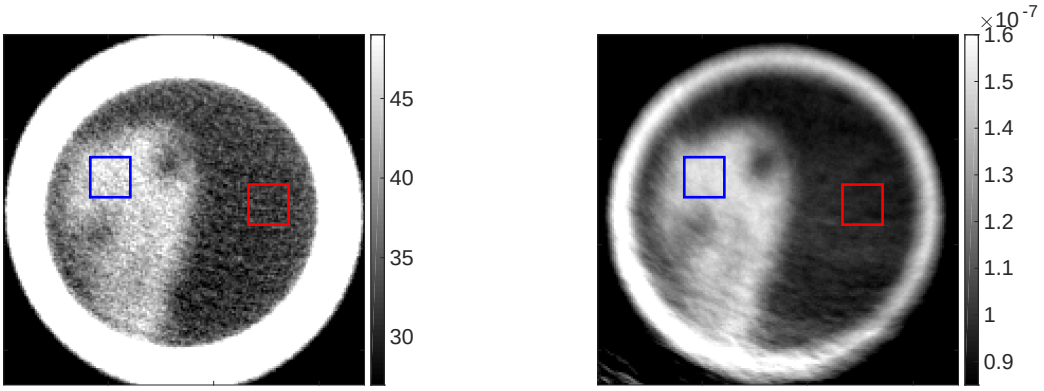

(a) Attenuation image **(b)** Phase image

Figure 3.41: CT slice of the Uric acid stone measured in water. The blue rectangle indicates the ROI in the object, the red one that of the background used for the calculation of the CNR.

each other. The error on the CNR value is calculated by error propagation of the error of the involved quantities. From the ROIs shown in figure 3.41, the CNR values that arise are listed in table 3.10. The most striking result is that at 60 kVp, the CNR in the phase shift image is almost three times larger than that of the attenuation image. The dark-field image, on the other hand, does not give an advantage over the attenuation image in terms of CNR at any of the used energies. It is worth noting that the CNR in the phase image deteriorates significantly for larger acceleration voltages, whereas the decrease in the other images is much smaller. Nevertheless, the phase image provides a larger CNR than both other images at all energies. Hence, phase-contrast CT could be used to localise Uric acid stones more easily and more accurately.

Table 3.10: CNR values for the same CT slice in attenuation, phase, and dark-field image. The corresponding ROIs are shown in figure 3.41.

Peak acceleration voltage	CNR values in Attenuation	Phase	Dark-field
60 kV	5.04 ± 0.14	14.50 ± 0.41	1.92 ± 0.08
70 kV	5.16 ± 0.15	9.50 ± 0.28	1.23 ± 0.06
80 kV	4.75 ± 0.14	7.33 ± 0.23	0.92 ± 0.06

Conclusion

Using the concept of Dual Energy phase-contrast Computed Tomography, the aim of this thesis was the identification and allocation of materials based on their attenuation coefficients, refrective index decrements and dark-field coefficients. For the allocation, an algorithm was implemented that, utilising CT measurements at different energies, allocates known materials to each pixel in a CT image. For that, calibration curves were measured for several materials at different energies and the material values – attenuation coefficient, refractive index decrement and dark-field coefficient – were averaged over a large region of interest. With the CT images of the object, the algorithm then solves a system of linear equations for volume proportions of the materials in every pixel. The algorithm proved to work well on a sample of plastic rods, where the proportions were averaged over many CT layers. In a more complex object made of mixed plastic swarf, which was not translationally invariant, the method could not truthfully allocate pixels to the right materials, because the results could not be averaged. From the calibration curves of the involved plastic materials, it is apparent that the material values do not differ enough, resulting in an impossible allocation of single pixels to one material. Transferring the method onto the clinical application of fat percentage estimation, the same problems occured. Hence, in objects where the allocation cannot be averaged over several layers, the algorithm remains inaccurate.

A more correct allocation of materials could be achieved by choosing different energies than those selected in this thesis. At other energies, the CT values of the materials could differ more and thus simplify the differentiation of materials via the allocation algorithm. Furthermore, using a monochromatic source instead of a polychromatic one or by adding filters, the spectra at both energies would truly be different, which could yield significant differences in the behaviour of the material values at both energies and thus facilitate the unambiguous allocation of materials.

In the second part of this thesis, the objective was to investigate physical quantities that characterise kidney stone minerals. The knowledge of the mineral composition of a patient's stones would be useful for more suitable treatment methods matching the pathology of each patient. In particular, Whewellite, Cystine and Brushite are minerals that are of special interest, as they are resistant to a common non-invasive shock wave treatment (ESWL). In the set of samples used in this thesis, there were five pure stones and five mixed stones that comprise more than one mineral. Among the pure stones, no Cystine or Whewellite stones were present, but Whewellite was contained in a few mixed stones. In order to find characteristic mineral parameters, the kidney stones were measured using phase-contrast radiography and phase-contrast CT in water-filled glass vials. The attenuation coefficients, refractive index decrements and dark-field coefficients of the stones were extracted from the CT images using an edge detection algorithm. For the phase-contrast radiography measurements, results from

the literature concerning dark-field and attenuation values of Uric acid in contrast to Oxalate stones could be confirmed. Carrying out CT measurements of the stones, it was investigated whether the refractive index decrement that is obtained only in tomographic measurements can be used as an additional property to characterise a material. The obtained CT values of the kidney stones were set in relation using scatter plots and forming quotients of the named quantities. An important result was that the CT values of the different pure minerals did not differ enough in the refractive index decrement and dark-field coefficient, in order to identify minerals based on these quantities. In the scatter plots, Uric acid, Weddellite and Brushite could be differentiated. This information can be used for clinical applications, as Brushite stones cannot be treated with ESWL, whereas Weddellite and Uric acid stones can. In addition to that, there is another non-invasive treatment method (chemolitholysis) that is only applicable for Uric acid stones. The quotients of the CT values did not yield any additional possibility to differentiate materials, mainly because they coincided for different minerals. Another result was that neither the material values obtained in CT nor the quotients of those quantities were the same for two pure Brushite samples from different patients. Therefore, one cannot find an absolute attenuation coefficient, refractive index decrement or dark-field coefficient that is assigned to a certain mineral. Lastly, phase-contrast CT has proven to give an advantage over conventional attenuation CT in terms of detection precision for Uric acid stones. The Contrast-to-Noise ratio of this mineral is significantly larger in the refractive index decrement image than in the attenuation image. This could improve the localisation process of Uric acid stones in clinical practice.

In further measurements, using a larger set of kidney stone samples of the same mineral from different patients, the inter-patient discrepancy of attenuation coefficient, refractive index decrement and dark-field coefficient should be examined. Furthermore, several Brushite stones from the same sample should be measured in order to find out whether intra-patient consistency for the CT material values is given. As an outlook for further measurements, the energy dependency of the attenuation coefficients, refractive index decrements and dark-field coefficients and their quotients should be investigated further. The measurements in this thesis have shown different energy dependencies of the materials, therefore a further investigation of this matter at more energies, preferably with monochromatic spectra, seems promising for possible characterisation of kidney stone minerals.

Appendix A

List of Figures

Appendix B

List of Tables

Appendix C

Bibliography

[1] T. R. C. Johnson. "Dual-Energy CT: General Principles". In: *American Journal of Roentgenology* 199.5 (2012), S3–S8. DOI: 10.2214/ajr.12.9116.

[2] T. R. C. Johnson et al. "Material differentiation by dual energy CT: initial experience". In: *European Radiology* 17.6 (2007), pp. 1510–1517. DOI: 10.1007/s00330-006-0517-6.

[3] C Fink et al. "Dual-energy CT angiography of the lung in patients with suspected pulmonary embolism: initial results". In: *RöFo-Fortschritte auf dem Gebiet der Röntgenstrahlen und der bildgebenden Verfahren*. Vol. 180. 10. © Georg Thieme Verlag KG Stuttgart· New York. 2008, pp. 879–883.

[4] H. K. Genant and D. Boyd. "Quantitative Bone Mineral Analysis Using Dual Energy Computed Tomography". In: *Investigative Radiology* 12.6 (1977), pp. 545–551.

[5] T. Kelly, N Berger, and T. Richardson. "DXA body composition: theory and practice". In: *Applied Radiation and Isotopes* 49.5-6 (1998), pp. 511–513.

[6] M. A. Laskey. "Dual-energy X-ray absorptiometry and body composition". In: *Nutrition* 12.1 (1996), pp. 45–51.

[7] R. Nord and R. Payne. "Body composition by dual-energy X-ray absorptiometry: a review of the technology". In: *Asia Pac J Clin Nutr* 4 (1995), pp. 167–71.

[8] A. Pietrobelli et al. "Dual-energy X-ray absorptiometry body composition model: review of physical concepts". In: *American Journal of Physiology-Endocrinology And Metabolism* 271.6 (1996), E941–E951.

[9] J. Clauser and M. Reinsch. "New Theoretical and Experimental Results in Fresnel Optics with Applications to Matter-Wave and X-Ray Interferometry". In: *Applied Physics B Photophysics and Laser Chemistry* 54.5 (1992), pp. 380–395. DOI: 10.1007/bf00325384.

[10] A. Momose et al. "Demonstration of X-Ray Talbot Interferometry". In: *Japanese Journal of Applied Physics* 42.Part 2, No. 7B (2003), pp. L866–L868. DOI: http://dx.doi.org/10.1143/JJAP.42.L866.

[11] T. Weitkamp et al. "X-ray phase imaging with a grating interferometer". In: *Optics Express* 13.16 (2005), p. 6296. DOI: 10.1364/opex.13.006296.

[12] F. Pfeiffer et al. "Phase retrieval and differential phase-contrast imaging with low-brilliance X-ray sources". In: *Nature Physics* 2.4 (2006), pp. 258–261. DOI: doi:10.1038/nphys265.

[13] D. G. A. Victoriano Romero Haluk Akpinar. "Kidney Stones: A Global Picture of Prevalence, Incidence, and Associated Risk Factors". In: *Reviews in Urology* 12.2/3 (2010), pp. 86–96. DOI: 10.3909/riu0459.

[14] P. Joseph et al. "Computerized Tomography Attenuation Value of Renal Calculus: Can It Predict Successful Fragmentation of the Calculus by Extracorporeal Shock Wave Lithotripsy? A Preliminary Study". In: *The Journal of Urology* (2002), pp. 1968–1971. DOI: 10.1097/00005392-200205000-00007.

[15] J. C. Williams et al. "Variability of renal stone fragility in shock wave lithotripsy". In: *Urology* 61.6 (2003), pp. 1092–1096. DOI: 10.1016/S0090-4295(03)00349-2.

[16] A. N. Primak et al. "Noninvasive Differentiation of Uric Acid versus Non–Uric Acid Kidney Stones Using Dual-Energy CT". In: *Academic Radiology* 14.12 (2007), pp. 1441–1447. DOI: 10.1016/j.acra.2007.09.016.

[17] K. Scherer et al. "Non-invasive Differentiation of Kidney Stone Types using X-ray Dark-Field Radiography". In: *Scientific Reports* 5 (2015), p. 9527. DOI: 10.1038/srep09527.

[18] W. Demtröder. *Experimentalphysik 2 - Elektrizität und Optik*. Springer Berlin Heidelberg, 2013. DOI: 10.1007/978-3-642-29944-5.

[19] H. Krieger. "Strahlungsarten und Strahlungsfelder". In: *Grundlagen der Strahlungsphysik und des Strahlenschutzes*. Wiesbaden: Vieweg+Teubner Verlag, 2012, pp. 168–217. DOI: 10.1007/978-3-8348-2238-3_1.

[20] D. Paganin. *Coherent X-Ray Optics*. Oxford University Press (OUP), 2006. DOI: 10.1093/acprof:oso/9780198567288.001.0001.

[21] A. H. Compton. "A quantum theory of the scattering of X-rays by light elements". In: *Physical review* 21.5 (1923), p. 483.

[22] W. C. Röntgen. "Über eine neue Art von Strahlen". In: *Annalen der Physik* 300.1 (1898), pp. 1–11. DOI: 10.1002/andp.18983000102.

[23] O. Dössel. *Bildgebende Verfahren in der Medizin*. Springer Nature, 2000. DOI: 10.1007/978-3-662-06046-9.

[24] H. Krieger. *Strahlungsquellen für Technik und Medizin*. Springer Nature, 2013. DOI: 10.1007/978-3-658-00590-0.

[25] H. Krieger. "Atombau". In: *Grundlagen der Strahlungsphysik und des Strahlenschutzes*. Springer Nature, 2012. Chap. 2, pp. 52–90. DOI: 10.1007/978-3-8348-2238-3.

[26] J. T. Bushberg et al. *The essential Physics of Medical Imaging*. Ed. by W. M. P. III. Williams & Wilkins, 1994.

[27] H. F. Talbot. "Facts relating to optical science". In: *The London and Edinburgh Philosophical Magazine and Journal of Science* IV.56 (1836), pp. 401–406.

[28] Lord Rayleigh. "On copying diffraction-gratings, and on some phenomena connected therewith". In: *Philosophical Magazine Series 5* 11.67 (1881), pp. 196–205. DOI: 10.1080/14786448108626995.

[29] W. B. Case et al. “Realization of optical carpets in the Talbot and Talbot-Lau configurations”. In: *Opt. Express* 17.23 (2009), pp. 20966–20974. DOI: 10.1364/OE.17.020966.

[30] A. Yan, X. Wu, and H. Liu. “A general theory of interference fringes in x-ray phase grating imaging”. In: *Medical Physics* 42.6 (2015), pp. 3036–3047. DOI: 10.1118/1.4921124.

[31] T. J. Suleski. “Generation of Lohmann images from binary-phase Talbot array illuminators”. In: *Applied Optics* 36.20 (1997), p. 4686. DOI: 10.1364/ao.36.004686.

[32] E. Lau. “Beugungserscheinungen an Doppelrastern”. In: *Annalen der Physik* 437.7-8 (1948), pp. 417–423. DOI: 10.1002/andp.19484370709.

[33] T. Weber. “Untersuchungen zur gitterbasierten Phasenkontrast-Röntgenbildgebung in polychromatischen Strahlungsfeldern”. PhD thesis. Friedrich-Alexander-Universität Erlangen-Nürnberg, 2013.

[34] V. Ludwig. *Directional dark-field imaging with a helical computed tomography scanning system*. IMPRS Minithesis. 2016.

[35] P. Bartl. “Phasenkontrast-Bildgebung mit photonenzählenden Detektoren”. PhD thesis. Friedrich-Alexander-Universität Erlangen-Nürnberg, 2010.

[36] G.-H. Chen et al. “Small-angle scattering computed tomography (SAS-CT) using a Talbot-Lau interferometer and a rotating anode x-ray tube: theory and experiments”. In: *Opt. Express* 18.12 (2010), pp. 12960–12970. DOI: 10.1364/OE.18.012960.

[37] M Bech et al. “Quantitative x-ray dark-field computed tomography”. In: *Physics in Medicine and Biology* 55.18 (2010), pp. 5529–5539. DOI: 10.1088/0031-9155/55/18/017.

[38] G. M. Blake and I. Fogelman. “Technical principles of dual energy x-ray absorptiometry”. In: *Seminars in nuclear medicine* 27.3 (1997), pp. 210–228.

[39] P. Stenner. “Quantitative Methoden in der Dual-Source-Computertomographie”. PhD thesis. Friedrich-Alexander-Universität Erlangen-Nürnberg, 2010.

[40] J. Radon. “Über die Bestimmung von Funktionen durch ihre Integralwerte längs gewisser Mannigfaltigkeiten.” In: *Ber. Saechs. Akad. Wiss. Leipzig, Math-Phys. Kl.,* 69 (1917), pp. 262–277.

[41] S. Ens. “Grundlagen der Computertomographie”. In: *Bewegungsdetektion und -korrektur in der Transmissions-Computertomographie*. Springer Nature, 2015, pp. 7–23. DOI: 10.1007/978-3-658-07693-1_2.

[42] T. M. Buzug. *Computed Tomography*. Springer Nature, 2008. DOI: 10.1007/978-3-540-39408-2.

[43] G. N. Ramachandran and A. V. Lakshminarayanan. “Three-dimensional Reconstruction from Radiographs and Electron Micrographs: Application of Convolutions instead of Fourier Transforms”. In: *Proceedings of the National Academy of Sciences* 68.9 (1971), pp. 2236–2240.

[44] D. Prell, Y. Kyriakou, and W. A. Kalender. “Comparison of ring artifact correction methods for flat-detector CT”. In: *Physics in Medicine and Biology* 54.12 (2009), pp. 3881–3895. DOI: 10.1088/0031-9155/54/12/018.

[45] K. T. Türk C. *Guidelines on Urolithiasis*. European Association of Urology. 2015.

[46] S. C. Müller. "Epidemiologie, instrumentelle Therapie und Metaphylaxe des Harnsteinleidens". In: *Deutsches Ärzteblatt* 101.19 (2004).

[47] C. Bach and N. Buchholz. "Shock Wave Lithotripsy for Renal and Ureteric Stones". In: *European Urology Supplements* 10.5 (2011), pp. 423–432. DOI: 10.1016/j.eursup.2011.07.004.

[48] http://www.mdpi.com/sensors/sensors-13-01319/article_deploy/html/images/sensors-13-01319f5-1024.png. 2017 (assessed January 17, 2017).

[49] R. C. Smith and M. Varanelli. "Diagnosis and management of acute ureterolithiasis: CT is truth". In: *American Journal of Roentgenology* 175.1 (2000), pp. 3–6.

[50] A. Graser et al. "Dual Energy CT Characterization of Urinary Calculi: Initial In Vitro and Clinical Experience". In: *Investigative Radiology* 43.2 (2008), pp. 112–119.

[51] H. Mitcheson et al. "Determination of the chemical composition of urinary calculi by computerized tomography." In: *The Journal of Urology* 130.4 (1983), pp. 814–819.

[52] M. R. Mostafavi, R. D. Ernst, and B. Saltzman. "Accurate Determination of Chemical Composition of Urinary Calculi by Spiral Computerized Tomography". In: *The Journal of Urology* (1998), pp. 673–675. DOI: 10.1097/00005392-199803000-00010.

[53] M.-F. Bellin et al. "Helical CT evaluation of the chemical composition of urinary tract calculi with a discriminant analysis of CT-attenuation values and density". In: *European radiology* 14.11 (2004), pp. 2134–2140.

[54] http://www.visiondummy.com/2014/04/draw-error-ellipse-representing-covariance-matrix/. 2017 (assessed March 10, 2017).

[55] http://www.reid.ai/2012/09/chi-squared-distribution-table-with.html. 2017 (assessed March 10, 2017).

[56] W. Metzger. *Statistical methods in data analysis*. Tech. rep. Nijmegen Univ. Fys. Lab., 2002.

Acknowledgements

There are many people whitout whom this thesis could not have been realised. I would like to thank them for their contributions:

Prof. Dr. Gisela Anton, thank you for the opportunity to work on this subject and for your support.

Prof. Dr. Bernd Wullich, thank you for the opportunity to conduct the study on the stones and for pushing ahead with the ethics commitee permission.

PD Dr. Thilo Michel, thank you for fruitful discussions and creative suggestions.

Dr. Georg Pelzer, a massive thank you for the great supervision, for answering all my questions, for your ideas and for helping me with the measurements.

Dr. Wencke Losensky, thank you for your interest in the study, for providing me so promptly with the stones and for explaining the urological side of the matter to me.

Jens Rieger, Florian Horn, Veronika Ludwig, thank you for helping me with the CT set-up, with the reconstruction of the CT images, with the edge-detection algorithm and just for your general helpfulness.

Maria Seifert, thank you so much for helping me with any problems and questions I have had concerning Matlab, understanding the physics of phase-contrast and interpreting my results. In particular, thanks for proof-reading my thesis so quickly and carefully.

Tobias Ziegler, thanks for being my number one proof-reader, statistics advisor and LaTeX-guru and for everything else.

Christian Hauke, Andrea Zang, and all other former/temporary inhabitants of room 213, thanks for the quick help with my questions and for the fun times!

The whole MedPhys group, thanks for the laid-back atmosphere and for the helpful suggestions in the meetings.

My family, thank you for your support throughout my whole life, I can never give back what you have given me.

Statutory Declaration

I declare that I have developed and written the enclosed Master's Thesis completely by myself, and have not used sources or means without declaration in the text. Any thoughts from others or literal quotations are clearly marked. The Master's Thesis was not used in the same or in a similar version to achieve an academic grading or is being published elsewhere.

Erlangen, March 23, 2017

Theresa Palm